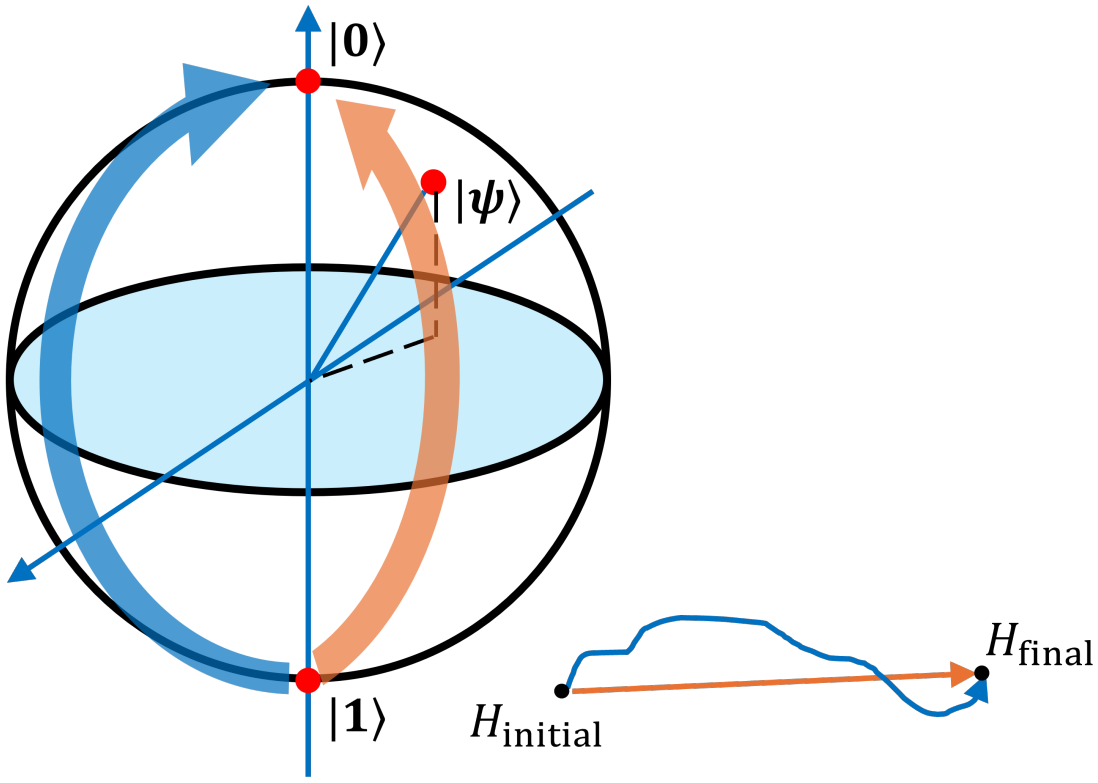

Implementation of Qubit Reset for Fixed-Frequency Transmons in Tunable-Coupler Architectures

Adiabatic and Shortcut-to-Adiabaticity Path in Qubit Reset

Master's thesis in Nanotechnology

ZIXIAN YAN

DEPARTMENT OF MICROTECHNOLOGY AND NANOSCIENCE
CHALMERS UNIVERSITY OF TECHNOLOGY
Gothenburg, Sweden 2024
www.chalmers.se

Master's thesis 2024

Implementation of Qubit Reset for Fixed-Frequency Transmons in Tunable-Coupler Architectures

ZIXIAN YAN

CHALMERS
UNIVERSITY OF TECHNOLOGY

Department of Microtechnology and Nanoscience
Quantum Technology Laboratory
Chalmers University of Technology
Gothenburg, Sweden 2024

Implementation of Qubit Reset for Fixed-Frequency Transmons in Tunable-Coupler Architectures
ZIXIAN YAN

Supervisor: Liangyu Chen, Giovanna Tancredi, Department of Microtechnology and Nanoscience
Examiner: Jonas Bylander, Department of Microtechnology and Nanoscience

Master's Thesis 2024
Department of Microtechnology and Nanoscience
Quantum Technology Laboratory
Chalmers University of Technology
SE-412 96 Gothenburg
Telephone +46 73 483 8375

Cover: Adiabatic Control

Typeset in LaTeX
Printed by Chalmers Reproservice
Gothenburg, Sweden 2024

Implementation of Qubit Reset for Fixed-Frequency Transmons in Tunable-Coupler Architectures
ZIXIAN YAN
Department of Microtechnology and Nanoscience
Chalmers University of Technology

Abstract

Unconditional and fast qubit reset is a key element to decrease algorithm computation time as the lifetime of the physical qubits continuously grows. For example, in quantum error correction (QEC), fast qubit reset in ancilla qubits is highly desired to accelerate the surface code algorithm. This thesis reports a qubit reset protocol utilizing a tunable coupler to transfer excitation from the qubit to the dedicated readout resonator in an architecture consisting of fixed-frequency transmons pairwise coupled by tunable couplers. The reset pulse is designed and optimized based on the Roland-Cerf protocol for resetting the $|e\rangle$-state adiabatically in a two-level system (TLS) with an adiabatic pulse, demonstrating an improvement in reset fidelity compared to linear pulse in simulation. By changing the pulse shape, the evolution follows the shortcut-to-adiabaticity (STA) path within some parameter regions, enabling faster and better qubit reset. For resetting $|f\rangle$-state, the numerical results also give adiabatic and STA pulse shapes similar to that given by the Roland-Cerf protocol in a two-level system, thus enabling us to model the $|f\rangle$-state reset model as an approximate TLS system. We verify our theoretical prediction by running the reset protocols on a 25-qubit chip. The experiment results show fast reset operations while keeping low reset errors, verifying the validity of the proposed pulses [1]. However, the presence of other qubits limits the reset fidelity, and therefore, frequency separation between coupled qubits should be a parameter to be carefully considered at the design stage.

Keywords: quantum computing, superconducting circuit, adiabatic theorem

Acknowledgements

I would like to thank my supervisors, Liangyu Chen and Giovanna Tancredi, and examiner, Jonas Bylander, for their full support and guidance in my Master's thesis. The experiment was mainly carried out by Liangyu Chen to validate my theory. For the theory and simulation part, I'd like to thank Simon Pettersson Fors and Tahereh Abad for their advice. I extend my gratitude to Mohammad H. Ansari and Xuexin Xu from Peter Grünberg Institute (PGI) for their help in block-diagonalization and effective Hamiltonian.

Zixian Yan, Gothenburg, October 2024

List of Acronyms

Below is the list of acronyms that have been used throughout this thesis listed in alphabetical order:

cQED	Circuit Quantum Electrodynamics
CR SWAP	Coupler-Resonator Swap
DC-SQUID	DC-Superconducting Quantum Interference Device
MBQC	Measurement-Based Quantum Computation
NPAD	Nonperturbative Analytical Diagonalization
QC SWAP	Qubit-Coupler Swap
QHO	Quantum Harmonic Oscillator
RC protocol	Roland-Cerf protocol
STA	Shortcut-To-Adiabaticity
SWT	Schrieffer–Wolff transformation
TLS	Two-Level System

Contents

List of Figures

List of Tables

1

Introduction

1.1 Quantum computing and quantum information

Quantum computing exploits the physical properties of quantum mechanical systems, such as superposition and entanglement, to perform computational tasks. The idea of using quantum systems to perform computation was first proposed by physicist Richard Feynman in 1982, motivated by difficulties in simulating physics on classical computers. For example, Feynman proposed that a spin wave in a lattice can simulate the Bose particles [2]. Then, in 1985, David Deutsch introduced the concept of a universal quantum computer and showed how such a machine would work by showcasing what is now known as Deutsch's algorithm [3]. This algorithm was generalized and proved to have exponential speedup over any deterministic classical algorithm [4, 5]. In 1994, Peter Shor demonstrated that a quantum algorithm tailored for prime factorization [6] would have been the fastest algorithm compared to any existing classical algorithm [7]. Similar to classical heuristic algorithms, quantum heuristic algorithms have also been proposed to solve combinatorial optimization problems [8–11].

In classical computing, the basic information processing unit is a bit with two possible logical states, 0 or 1. The counterpart of a bit in quantum computing is a **quantum bit**, or a **qubit**, representing any possible superposition of $|0\rangle$ and $|1\rangle$. Research on 3-level quantum system (**qutrit**) and d-level quantum system (**qudit**) as a basic unit has been proposed to allow larger dimensions in Hilbert space and are found to be useful in magic-state distillation [12], topological quantum computer [13] and quantum key distribution [14].

Any quantum algorithm can be expressed as a quantum circuit where the qubits represent the data, with the qubits being prepared in an initial state before being processed. **Quantum gates** then act on the qubits to control quantum states. At the end of the computation, the qubit is read out by a **measurement operation**.

1.2 Superconducting quantum computing

Many physical implementations are currently being investigated to realize a real quantum computer based on different types of material or matter: ion traps, su-

perconducting circuits, photons, and Rydberg atoms. Superconducting circuits are one of the prominent candidates due to the superior control speed and relatively good scalability compared to other platforms and are widely adopted by many tech companies [15, 16] and institutions [17–20].

Superconducting circuits can exhibit quantum-mechanical effects on a macroscopic level. An early experiment in 1985 showed indirect evidence of discrete energy levels indicated by phase difference across the barrier of a Josephson junction when irradiated with microwave signals [21]. In the following years, scientists observed energy-level splitting in the superconducting electrical circuit [22] and successfully performed coherent quantum control in a Cooper-pair box [23]. This suggested that the two charge states could be used as computational qubit states, with the Cooper-pair box referred to as a type of charge qubit. Many other types of superconducting circuit-based qubits have been proposed, including flux qubits [24, 25] and phase qubits [26, 27]. Among them, the transmon qubit stands out for its insensitivity to charge noise or external flux change [28].

Superconducting quantum processors have evolved rapidly in recent years with the growing number of physical qubits and many scientific breakthroughs. In 2014, John Martinis group at UCSB reported that for the first time, the logical gates could be implemented with fidelity, reaching the threshold for universal quantum computing in a superconducting circuit-based platform [29]. The following year, they successfully demonstrated how to detect bit-flip errors and protect the qubits from the environment on a chip of nine physical qubits placed in a linear chain [30]. In the same year, IBM achieved single-qubit error detection by measuring syndrome qubits on a planar chip [31]. In 2019, Google claimed that their 53-qubit Sycamore processor could execute a random quantum circuit sampling algorithm in only polynomial time, giving exponential speedup over classical computers [32]. The experimental implementation of correction codes was further developed, and it was experimentally verified that the surface code could reduce logical errors on a 72-qubit chip [16].

1.3 Qubit reset

In quantum computing, qubit reset brings the qubit from any arbitrary state back to its ground state. Qubit reset can be either conditional or unconditional. In conditional reset protocols, qubits are reset with active coherent driving conditioned on the measurement outcome [33–35]. The major issue in conditional resets is that the classical feedback time could take up significant computational time, greatly limiting the runtime of quantum algorithms. This constitutes a major limitation in surface code, where measurements and resets are frequently executed. On the other hand, unconditional reset operations are not conditioned on the measured outcomes; they typically take advantage of qubit decay or introduce external coupling or control [36–40].

Here, we demonstrate a qubit reset protocol on the first excited state $|e\rangle$ and the

second excited state $|f\rangle$, tailored for a fixed transmon and tunable coupler architecture without any additional coupling or control line. Our scheme demonstrated that it can be easily implemented in large-scale quantum processors. The protocol uses flux-tunable couplers as media to remove the qubit population in higher states [41] and let it decay through the lossy readout resonator. In the qubit-coupler swapping, the qubit state is unconditionally and adiabatically reset to the ground state without any classical feedback and using only flux control.

1.4 Objectives

This thesis mainly focuses on achieving the following objectives:

1. Deriving a closed form, analytical pulse to accelerate the adiabatic control for the qubit $|e\rangle$-state reset.
2. Numerically derive the adiabatic pulse for qubit $|f\rangle$-state reset.
3. Using non-perturbative analytical diagonalization and Schrieffer–Wolff transformation to derive an effective two-level system Hamiltonian in modeling the qubit $|f\rangle$-state reset.
4. Analytically derive the pulse to accelerate the adiabatic control for the qubit $|f\rangle$-state reset using the effective Hamiltonian.
5. Show the implementation of the proposed adiabatic pulse in both simulation and experiment.

1.5 Chapters Description

This thesis is outlined as follows: Chapter 2 briefly introduces the definition of qubits, quantum gates and quantum measurement, and describes the theory of circuit quantum electrodynamics. Chapter 2 is also devoted to deriving the analytical expression of adiabatic pulse based on Roland and Cerf protocol for a two-level system in $|e\rangle$-state reset, and we further extend this reset protocol to $|f\rangle$-state reset by deriving an effective two-level system using block diagonalization techniques. Chapter 3 presents the experimental setup and the results are shown in Chapter 4. The thesis is concluded with a summary and discussion in Chapter 5.

2

Theory and Modeling

2.1 Brief introduction to quantum computing

In this section, we briefly introduce quantum computing based on the circuit model. The circuit model comprises four key elements: qubits, state preparation, quantum gate operations and measurements. Any quantum state $|\psi\rangle$ of a qubit in a closed system can be mapped to a point at the Bloch sphere, represented by two coordinates θ and γ:

$$|\psi\rangle = \cos\left(\frac{\theta}{2}\right)|0\rangle + e^{i\gamma}\sin\left(\frac{\theta}{2}\right)|1\rangle\,, \tag{2.1}$$

where the state $|0\rangle$ sits at the north pole and the state $|1\rangle$ sits at the south pole. In this thesis, we adopt the convention that the states $|0\rangle$, $|1\rangle$, $|2\rangle$ and the states $|g\rangle$, $|e\rangle$, $|f\rangle$ are treated as interchangeable.

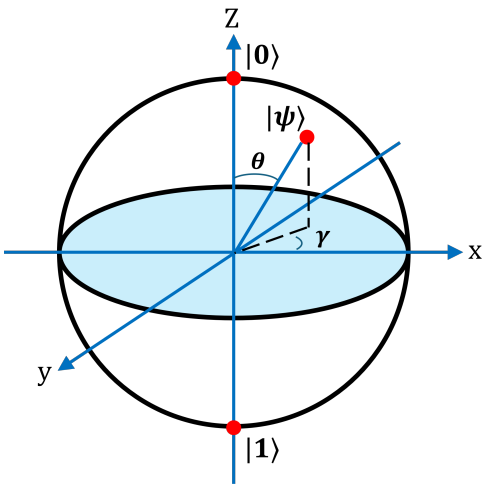

Figure 2.1: Bloch sphere representation of an arbitrary quantum state $|\psi\rangle$. A quantum state can be interpreted as a state vector pointing to the surface of the Bloch sphere. The coordinates θ and γ denote the angle between the state vector and z-axis and between the state vector's projection onto the x-y equator and the x-axis.

To process the quantum information, the qubit is first initialized to a state $|\psi_0\rangle$, followed by a set of designed quantum gates in sequence, denoted by unitary operation

U_i for each gate and arriving at a new state $|\psi_t\rangle$,

$$|\psi_t\rangle = \prod_i U_i |\psi_0\rangle . \tag{2.2}$$

Since all the quantum gates are unitary, the gate sequence is essentially equivalent to only one unitary operation U. From the view of hardware, the gate operation U is designed and engineered based on the physical system described by a Hamiltonian H, given the Schrödinger equation:

$$i\frac{\partial U(t)}{\partial t} = H(t)U(t). \tag{2.3}$$

Thus, by solving this quantum dynamics, the unitary is obtained:

$$U = e^{-i\int_0^T H(t)dt}. \tag{2.4}$$

After gate operations, we perform measurements to extract the information from the qubit at the end of the quantum circuit. For example, a projective measurement in the z basis causes the quantum state $|\psi\rangle$ collapse to either $|0\rangle$ or $|1\rangle$. It is worth noticing that the measurement is a non-unitary, irreversible process, and therefore, the state cannot be recovered after being measured.

2.2 Circuit quantum electrodynamics

Circuit quantum electrodynamics (cQED) studies the interaction between light and artificial matter, analogous to cavity quantum electrodynamics, where an atom and light are made to interact by placing the atom inside the cavity [42, 43]. Depending on the physical size of the physical circuit elements compared to the wavelength of the relevant propagating electromagnetic field, there are two types of circuit components. For the lump elements, which are smaller than the radiation wavelength, the effect of propagating radiation field on the circuit is so small that the information is stored only in the circuit elements and can be simplified as a lumped circuit mathematically. For the distributed elements, on the contrary, it is necessary to include the radiation field as part of the model [44, 45].

2.2.1 Quantum harmonic oscillator: LC circuit

Using the theory of cQED, we can derive any system Hamiltonian given circuit with finite elements. Following the formalism outlined in previous work [44–47], we present a simple example to show how to derive the Hamiltonian. The simplest man-made atom in the form of an electrical circuit is an LC circuit, consisting of only two lump elements: a capacitor and an inductor. In the lumped-circuit model, each lump element connects two nodes a and b and therefore can be modeled as a branch described by two circuit quantities: the voltage $V(t)$ between node a and b and the current $I(t)$ flowing through a to b. Each element stores energy $E(t)$:

$$E(t) = \int_{-\infty}^{t} V(t')I(t')dt'. \tag{2.5}$$

In a capacitor, the energy stored in the electric field with capacitance C and charges $Q(t)$ is:

$$E_C(t) = \int_{-\infty}^{t} \frac{Q(t')}{C} \cdot \frac{dQ(t')}{dt'} dt' = \frac{Q^2(t)}{2C}. \tag{2.6}$$

With the relations $V(t) = Q(t)/C$ and $V(t) = d\Phi(t)/dt$, the energy can be expressed in $\Phi(t)$:

$$E_C(t) = \frac{C\dot{\Phi}(t)}{2}. \tag{2.7}$$

In an inductor, the energy stored in the magnetic field with inductance with L:

$$E_L(t) = \int_{-\infty}^{t} \frac{d\Phi(t')}{dt'} \cdot \frac{\Phi(t')}{L} dt' = \frac{\Phi^2(t)}{2L}. \tag{2.8}$$

The branch flux $\Phi_C(t)$ of the capacitor C is exactly the node flux $\Phi(t)$, and Kirchhoff's law tells us that the net sum of the branch flux in an enclosed loop is some constant flux Φ_{cons}

$$\sum_{b \in \text{elements}} \Phi_b(t) = \Phi_{\text{const}}. \tag{2.9}$$

Therefore, we have:

$$\begin{aligned} \Phi_C(t) + \Phi_L(t) &= \Phi_{\text{const}} \\ \dot{\Phi}_C(t) &= -\dot{\Phi}_L(t). \end{aligned} \tag{2.10}$$

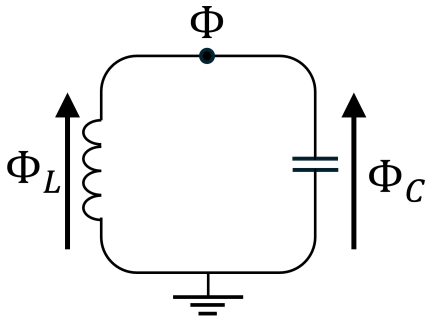

Figure 2.2: LC circuit. Φ_C and Φ_L denote flux across the capacitor C and the inductor L. The node flux Φ is defined as $\Phi = \Phi_L$

Now, we can write down the Lagrangian as a function of the node flux $\Phi(t)$ for the LC circuit before obtaining the system Hamiltonian:

$$\mathcal{L} = \frac{C}{2}\dot{\Phi}_C^2(t) - \frac{1}{2L}\Phi_L^2(t) = \frac{C}{2}\dot{\Phi}^2(t) - \frac{1}{2L}\Phi^2(t). \tag{2.11}$$

The conjugate variable $Q(t)$ can be derived by:

$$Q(t) = \frac{\partial \mathcal{L}}{\partial \dot{\Phi}} = C\dot{\Phi}(t). \tag{2.12}$$

The system Hamiltonian in the Q, Φ representation is readily written:

$$H(t) = Q\dot{\Phi} - \mathcal{L} = \frac{1}{2C}Q^2(t) + \frac{1}{2L}\Phi^2(t). \tag{2.13}$$

In the first quantization, canonical communication is imposed to the coordinates $Q(t)$ and $\Phi(t)$, corresponding to operators $\hat{\Phi}$ and $\hat{Q}$,

$$[\hat{\Phi}(t), \hat{Q}(t)] = i\hbar, \tag{2.14}$$

leading to the Hamiltonian in a new representation:

$$\hat{H}(t) = \frac{1}{2C}\hat{Q}^2(t) + \frac{1}{2L}\hat{\Phi}^2(t). \tag{2.15}$$

By introducing the annihilation and creation operators in the second quantization, the transformation from $\hat{Q}$, $\hat{\Phi}$ to $\hat{a}$ and $\hat{a}^\dagger$ is defined as:

$$\hat{\Phi} = \Phi_{\text{zpf}}(\hat{a} + \hat{a}^\dagger), \tag{2.16}$$

$$\hat{Q} = Q_{\text{zpf}}(\hat{a} - \hat{a}^\dagger), \tag{2.17}$$

where Φ_{zpf} and Q_{zpf} denotes the standard deviation of flux and charge coordinates. The Hamiltonian for the LC circuit in terms of a and $a^\dagger$ is exactly a description of a quantum harmonic oscillator (QHO):

$$\hat{H}(t) = \hbar\omega_r \left(\hat{a}^\dagger\hat{a} + \frac{1}{2}\right), \tag{2.18}$$

with frequency

$$\omega_r = \sqrt{\frac{1}{LC}}. \tag{2.19}$$

The Hamiltonian in Eq. (2.18) indicates that the eigenenergies of $H(t)$ are equispaced by $\hbar\omega_r$, and, by replacing $a^\dagger a$ with number operator $n = a^\dagger a$, we get

$$\boxed{\hat{H}(t) = \hbar\omega_r \left(n + \frac{1}{2}\right)}. \tag{2.20}$$

2.2.2 Quantum anharmonic oscillator: transmon

The equal spacing of $\hbar\omega_r$ between energy levels in the QHO spectrum makes it a bad choice for a physical qubit since leakage out of computational basis $|0\rangle$ ($|g\rangle$) and $|1\rangle$ ($|e\rangle$) always exists, and an ideal physical qubit should be approximately a two-level system (TLS). To this end, nonlinearity is added to the LC circuit to isolate the lowest energy levels well enough from higher levels. This is achieved by replacing

the linear inductor with a Josephson junction J.

A Josephson junction features two superconductors with an insulator in between. The tunneling effect of Cooper pairs with charge $2e$ in the Josephson junction gives rise to the current flowing across the junction. Depending on the presence of the external voltage, there are two types of tunneling currents explained by the DC Josephson effect and AC Josephson effect [48–50]. The DC Josephson current without externally applied voltage across the junction can be expressed as:

$$I = I_0 \sin \varphi, \tag{2.21}$$

where φ is the phase difference between the two islands and I_0 is the critical current. When a voltage V is applied, the Josephson current I oscillates because of the time-dependent $\varphi = \varphi(t)$. This is known as the AC Josephson effect, represented by the relation between voltage V and phase φ:

$$V = \frac{\hbar}{2e}\dot{\varphi}. \tag{2.22}$$

With Eq. (2.21) and Eq. (2.22), the energy stored in a Josephson junction is:

$$E = \int_{-\infty}^{t} V(t')I(t')dt' = \frac{I_0\hbar}{2e}\int_{-\infty}^{t} \dot{\varphi}\sin\varphi dt' = -E_J \cos\varphi. \tag{2.23}$$

The parameter $E_J = I_0\hbar/2e$ represents the energy induced by critical current I_0 flowing through a Josephson inductance L_J:

$$E_J = \frac{I_0\hbar}{2e} = \frac{1}{2}L_J I_0^2, \tag{2.24}$$

$$L_J = \frac{\hbar}{eI_0}. \tag{2.25}$$

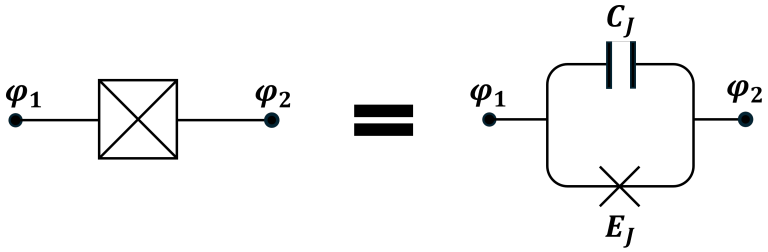

Figure 2.3: Josephson junction with characteristic capacitance C_J and Josephson energy E_J. The phase φ across the junction is the phase difference between φ_1 and φ_2 in the two islands.

Unlike unpaired electrons, a Cooper pair (two bounded electrons) behaves as bosons, meaning that any number of Cooper pairs can penetrate the barrier and condense into the ground state on the other side. Therefore, we can define N as the number of Cooper pairs on one side of the junction related to the charge Q by [44]

$$Q = -2eN. \tag{2.26}$$

To interpret the role of a Josephson junction in the electric circuit, we here introduce new conjugate variables, the number of Cooper pairs N and phase φ, satisfying $[\varphi, N] = i$:

$$N = -\frac{Q}{2e}, \tag{2.27}$$

$$\varphi = \frac{2\pi\Phi}{\Phi_0}. \tag{2.28}$$

The rate of the coupling between $|N\rangle$ and $|N+1\rangle$ is [44]:

$$H_J = -E_J \cos\varphi, \tag{2.29}$$

together with the capacitance, the system Hamiltonian reads:

$$H = 4E_C N^2 - E_J \cos\varphi. \tag{2.30}$$

In the kinetic term, E_C is the energy needed per Cooper pair, and N is the amount of Cooper pairs in the Josephson tunneling, and the second term accounts for the linearity in the potential. To see this, we can expand the cosine term ($\cos x \approx 1 - x^2/2 + x^4/24$) and drop the constant:

$$H \approx 4E_C N^2 + \frac{1}{2}E_J\varphi^2 - \frac{1}{24}E_J\varphi^4. \tag{2.31}$$

The first two terms form a QHO as the potential is a quadratic function in φ, but with the third term QHO, the potential is modified, and the system is no longer a QHO. It becomes more clear if we express the third term in Eq. (2.31) in terms of ladder operators (with φ_{zpf} denotes the zero-point fluctuation):

$$\varphi = \varphi_{\text{zpf}}(a + a^\dagger), \tag{2.32}$$

$$\varphi_{\text{zpf}} = \left(\frac{2E_C}{E_J}\right)^{\frac{1}{4}} \tag{2.33}$$

Thus, the nonlinear term $H_{\text{nl}} = -(E_J/24)\varphi^4$ in potential reads:

$$H_{\text{nl}} = -\frac{E_C}{12}(a + a^\dagger)^4, \tag{2.34}$$

keeping only excitation-conserved terms, we have [46]:

$$H_{\text{nl}} \approx \frac{\alpha}{2}a^\dagger a^\dagger a a + \alpha a^\dagger a, \tag{2.35}$$

where $\alpha = -E_C$ is the anharmonicity. The full Hamiltonian for a fixed-frequency charge qubit is:

$$\boxed{H = \hbar\omega_0 a^\dagger a + \frac{\hbar\alpha}{2}a^\dagger a^\dagger a a}, \tag{2.36}$$

with the resonant frequency $\omega_0 = \sqrt{8E_C E_J} - E_C$ and anharmonicity $\alpha = -E_C$. Now that we have a Hamiltonian with only non-zero diagonal terms, it is easy to compare the frequency required for the $|0\rangle$ - $|1\rangle$ transition and the $|1\rangle$ - $|2\rangle$ transition:

$$\omega_{01} = \omega_0, \tag{2.37}$$

$$\omega_{12} = \omega_0 + \alpha. \tag{2.38}$$

Therefore, this shift in transition frequency by α makes this system an approximate TLS. The ratio of Josephson energy E_J over capacitive energy E_C describes how anharmonic this system is:

$$\frac{|\alpha|}{|\omega_0|} = \frac{1}{|\sqrt{8E_J/E_C} - 1|}. \tag{2.39}$$

One might think that a large capacitive energy $E_C \gg E_J$ makes a good qubit due to large nonlinearity, but the system is more prone to charge noise in this regime. Thus, one needs to have a tradeoff between good anharmonicity and good insensitivity. Unlike early charge qubits such as a Cooper-pair box in the $E_C \gg E_J$ regime, the transmon qubit is almost insensitive to charge noise. This is achieved by adding a large shunt capacitance, making the transmon less sensitive to change in charge number [28, 45].

2.2.3 Tunable transmon

In our architecture, two transmon qubits are coupled together via a tunable transmon. In the tunable transmon, the single Josephson junction is replaced by a DC superconducting quantum interference device (DC-SQUID), a closed loop with two Josephson junctions. This tunable transmon is often referred to as the coupler throughout this thesis

In a ring made of superconductor, the net magnetic flux Φ_{net} threading through it is discrete and can only be multiples of $\Phi_0 = h/(2e)$:

$$\Phi_{\text{net}} = \sum_i \Phi_i = n\Phi_0. \tag{2.40}$$

By multiplying $2\pi/\Phi_0$, the reduced flux in terms of phase is:

$$\varphi_{\text{net}} = \sum_i \varphi_i = 2\pi n. \tag{2.41}$$

Consider a transmon with two identical Josephson junctions instead of one, each with capacitance C_J and Josephson energy E_J. The Hamiltonian for such a system in terms of phases $\varphi_{J_1} = 2\pi\Phi_{J_1}/\Phi_0$ and $\varphi_{J_2} = 2\pi\Phi_{J_2}/\Phi_0$ across two junctions is the sum of capacitive energy T and inductive energy V:

$$T = \frac{1}{2}\frac{C_J}{(2e)^2}\dot{\varphi}_{J_1}^2 + \frac{1}{2}\frac{C_J}{(2e)^2}\dot{\varphi}_{J_2}^2 = \frac{1}{4E_C}\dot{\varphi}_{J_1}^2 + \frac{1}{4E_C}\dot{\varphi}_{J_2}^2, \tag{2.42}$$

$$V = -E_J\cos\varphi_{J_1} - E_J\cos\varphi_{J_2}, \tag{2.43}$$

with the condition imposed by flux quantization

$$\varphi_{\text{ext}} - \varphi_{J_1} + \varphi_{J_2} = 2\pi n. \tag{2.44}$$

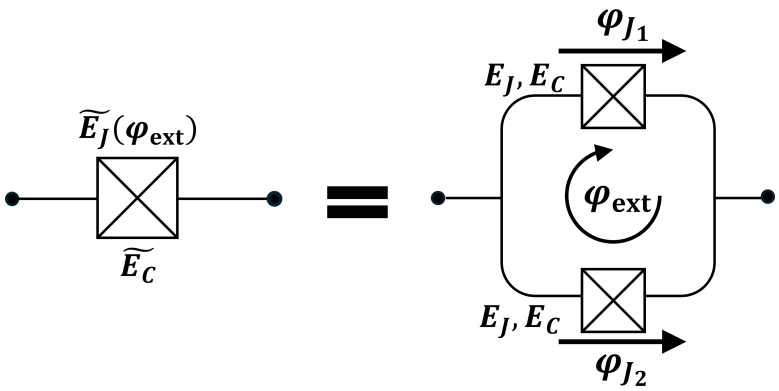

Figure 2.4: A DC-SQUID consisting of two identical Josephson junctions, both with Josephson energy E_J and capacitance energy E_C. The frequency is tuned by changing the external flux Φ_{ext} and the phase φ_{ext} changes accordingly. A DC-SQUID is equivalent to a single Josephson junction.

We can write down the Lagrangian as a function of φ_{ext} and $\varphi = \varphi_{J_2} - \varphi_{J_1}$:

$$\begin{aligned}\mathcal{L} &= T - V \\ &= \frac{1}{4E_C}\left(\frac{\dot{\varphi}_{\text{ext}} - \dot{\varphi}}{2}\right)^2 + \frac{1}{4E_C}\left(\frac{\dot{\varphi}_{\text{ext}} + \dot{\varphi}}{2}\right)^2 + E_J\left[\cos\left(\frac{\varphi_{\text{ext}} - \varphi}{2}\right) + \cos\left(\frac{\varphi_{\text{ext}} + \varphi}{2}\right)\right],\end{aligned} \tag{2.45}$$

and we can exclude the external flux-dependent terms contributing to the kinetic energy, arriving at

$$\mathcal{L} \approx \frac{1}{8E_C}\dot{\varphi}^2 + E_{2J}\cos(\varphi_{\text{ext}})\cos(\varphi), \tag{2.46}$$

where $E_{2J} = 2E_J$. The conjugate variable of the phase φ is obtained by ($E_{2C} = 4e^2/2(2C) = E_C/2$):

$$N = \frac{\partial \mathcal{L}}{\partial \dot{\varphi}} = \frac{1}{8E_{2C}}\dot{\varphi}, \tag{2.47}$$

leading to the Hamiltonian H for tunable transmon by definition:

$$H = N\dot{\varphi} - \mathcal{L} = 4E_{2C}N^2 - E_{2J}\cos(\varphi_{\text{ext}})\cos(\varphi). \tag{2.48}$$

By looking at the Hamiltonian in Eq. (2.48), a DC-SQUID is equivalent to a single Josephson junction described by Eq. (2.30), with charging energy $\tilde{E}_C = E_{2C}$ and coupling energy $\tilde{E}_J(\varphi_{\text{ext}}) = E_{2J}\cos(\varphi_{\text{ext}})$. This way, we can directly write down the Hamiltonian after the second quantization:

$$H_{SQ} = \omega_r(\varphi_{\text{ext}})a^\dagger a + \frac{\alpha}{2}a^\dagger a^\dagger a a, \tag{2.49}$$

where the resonant frequency ω_r and qubit anharmonicity α are:

$$\omega_r(\Phi_{\text{ext}}) = \sqrt{8E_{2C}E_{2J}\cos(2\pi\Phi_{\text{ext}}/\Phi_0)} - E_{2C}, \tag{2.50}$$

$$\alpha = -E_{2C}. \tag{2.51}$$

Hence, the tunability is inferred by external flux Φ_{ext} as an extra degree of freedom. In reality, a typical transmon also includes a gate capacitor and voltage source connecting to the superconductor island, which is also connected to a reservoir supplying Cooper pairs via a Josephson junction on the other side (Appendix A.1).

2.3 Adiabatic theorem

Adiabatic control ensures qubit reset with high fidelity and high robustness but at the cost of slow operation. To accelerate this process, the adiabatic condition is often imposed in the design of quantum operations. In this section, we review the adiabatic condition derived by assuming a perfect adiabatic process. Furthermore, to derive an analytical pulse satisfying the adiabatic condition, we often need to extract an effective Hamiltonian from a large system. We review Kato's adiabatic theorem, which states that in the adiabatic process, the relevant eigenstates can be isolated from all other states, followed by the mathematical formalism of obtaining effective Hamiltonian spanned by low-energy eigenstates given in Ref. [51].

2.3.1 Adiabatic condition

If a quantum mechanical system is initially in an eigenstate at time $t = 0$ and the condition affecting it changes slowly enough, the system will always stay in this eigenstate during the process. The quantum description of this process can be outlined as follows: the quantum state $|\psi(t)\rangle$ governed by a non-degenerate Hamiltonian $H(t)$ evolves from some kth initial eigenstate $|\psi_k(0)\rangle$ of $H(0)$, to a final state $|\psi_k(T)\rangle$ which is also the kth eigenstate of $H(T)$.

Here, we give a simple proof for approximate quantum adiabatic condition following work in Ref. [52]. The time-dependent Hamiltonian $H(t)$ at any time t satisfies

$$H(t)\,|\psi_n(t)\rangle = E_n(t)\,|\psi_n(t)\rangle\,. \tag{2.52}$$

Therefore, the Hamiltonian can be expanded on the eigenbasis:

$$H(t) = \sum_n E_n(t)|\psi_n(t)\rangle\langle\psi_n(t)|, \tag{2.53}$$

where $E_n(t)$ and $|\psi_n(t)\rangle$ are the eigenenergy and eigenstate of n-th energy level. The time-evolution of the state $|\Psi(t)\rangle$ is governed by $H(t)$:

$$\frac{\partial\,|\Psi(t)\rangle}{\partial t} = -iH(t)\,|\Psi(t)\rangle\,. \tag{2.54}$$

We expand the state $|\Psi(t)\rangle$ as a superposition of many eigenstates $|\psi(t)\rangle$ by multiplying $I = \sum_n |\psi_n(t)\rangle\langle\psi_n(t)|$:

$$|\Psi(t)\rangle = \sum_n \langle\psi_n(t)|\Psi(t)\rangle\, |\psi_n(t)\rangle = \sum_n C_n(t)\, |\psi_n(t)\rangle\,, \tag{2.55}$$

and the LHS of Eq. (2.54) becomes:

$$\frac{\partial\, |\Psi(t)\rangle}{\partial t} = \sum_n \left(\partial_t C_n(t)\, |\psi_n(t)\rangle + C_n(t)\partial_t\, |\psi_n(t)\rangle\right), \tag{2.56}$$

while the RHS becomes:

$$-iH(t)\, |\Psi(t)\rangle = -i\sum_n C_n(t)E_n(t)\, |\psi_n(t)\rangle\,. \tag{2.57}$$

Equating Eq. (2.56) and Eq. (2.57), we get:

$$\sum_n \left(\partial_t C_n(t)\, |\psi_n(t)\rangle + C_n(t)\partial_t\, |\psi_n(t)\rangle\right) = -i\sum_n C_n(t)E_n(t)\, |\psi_n(t)\rangle\,, \tag{2.58}$$

By left-multiplying $\langle\psi_m(t)|$, Eq. (2.58) becomes

$$\frac{\partial C_m(t)}{\partial t} + C_m(t)\langle\psi_m(t)|\dot{\psi_m}(t)\rangle + \sum_{n\neq m} C_n(t)\langle\psi_m(t)|\dot{\psi_n}(t)\rangle = -iC_m(t)E_m(t). \tag{2.59}$$

From $\partial_t(\langle\psi_m|\, H\, |\psi_n\rangle) = \partial_t(E_n\langle\psi_m|\psi_n\rangle) = 0$, we can then write

$$\begin{aligned}\partial_t(\langle\psi_m|\, H\, |\psi_n\rangle) &= \langle\dot{\psi_m}|H\, |\psi_n\rangle + \langle\psi_m|\, \dot{H}\, |\psi_n\rangle + \langle\psi_m|\, H|\dot{\psi_n}\rangle,\\ 0 &= E_n\langle\dot{\psi_m}|\psi_n\rangle + E_m\langle\psi_m|\dot{\psi_n}\rangle + \langle\psi_m|\, \dot{H}\, |\psi_n\rangle\,.\end{aligned} \tag{2.60}$$

This gives

$$\langle\psi_m|\dot{\psi_n}\rangle = \frac{\langle\psi_m|\, \dot{H}\, |\psi_n\rangle}{E_n - E_m}, \tag{2.61}$$

for $m \neq n$. From Eq. (2.59) and Eq. (2.61), the differential equation for the time derivative of complex amplitude C_m is given by:

$$\frac{\partial C_m}{\partial t} = -C_m\langle\psi_m|\dot{\psi_m}\rangle - iC_mE_m - \frac{\langle\psi_m|\, \dot{H}\, |\psi_n\rangle}{E_n - E_m}. \tag{2.62}$$

In an ideal, perfect adiabatic process, we can impose the third term in Eq. (2.62) to be 0:

$$\boxed{\frac{\langle\psi_m|\, \dot{H}\, |\psi_n\rangle}{E_n - E_m} \to 0.} \tag{2.63}$$

A more widely used adiabatic condition for evolution with duration T is similar to Eq. (2.63) [53]:

$$\boxed{\frac{\max\limits_{0\leq t\leq T} \langle\psi_m(t)|\, \dot{H}\, |\psi_n(t)\rangle}{\min\limits_{0\leq t\leq T} |E_n(t) - E_m(t)|^2} \ll 1.} \tag{2.64}$$

In other words, for an adiabatic process, the time scale for system change is supposed to be as large as possible compared to the energy gap between two non-degenerate states. If this condition in Eq. (2.63) is fulfilled, Eq. (2.62) becomes:

$$\frac{\partial C_m}{\partial t} = -C_m\langle\psi_m|\dot{\psi_m}\rangle - iC_mE_m. \tag{2.65}$$

The differential equation in Eq. (2.65) can be immediately solved:

$$\begin{aligned} C_m(t) &= e^{-\int_0^t\langle\psi_m(t')|\dot{\psi}_m(t')\rangle dt'}e^{-i\int_0^t E_m(t')dt'} \\ &= e^{i\theta_m(t)}e^{i\gamma_m(t)}, \end{aligned} \tag{2.66}$$

where $\theta_m(t) \equiv i\int_0^t\langle\psi_m(t')|\dot{\psi}_m(t')\rangle dt'$ is the Berry phase and $\gamma_m(t) \equiv -\int_0^t E_m(t')dt'$ is the dynamical phase. The complex amplitude in Eq. (2.66) indicates that in a perfect adiabatic process starting with an eigenstate $|\psi_n\rangle$, there is no transition to other eigenstates and a phase is accumulated in the state $|\psi_n\rangle$.

2.3.2 Kato's adiabatic theorem

Kato's adiabatic theorem describes the evolution of a subspace in the full system and gives the bound of adiabatic gate fidelity (how adiabatic a real evolution can be). Kato gave the formalism of the adiabatic theorem from the view of finding an adiabatic Hamiltonian H_a that can generate a perfect adiabatic evolution [54]. Here, we briefly introduce this theorem.

Suppose that a non-degenerate Hamiltonian $H(t)$ consists of two energy bands, one with the d lowest eigenstates $\mathcal{P} = \{|\psi_i(t)\rangle\}_{i=1}^d$ relevant to the adiabatic evolution and the other with the rest of the spectrum that is separated by a gap $\Delta(t)$. We can define the time-dependent projection denoted by $P(t)$ that projects some quantum state onto the relevant eigensubspace (the lower band):

$$P(t) = \sum_{i=1}^{d}|\psi_i(t)\rangle\langle\psi_i(t)|, \tag{2.67}$$

Now, imagine that a perfect adiabatic evolution $U_a(t)$ is generated by an adiabatic Hamiltonian $H_a(t)$, via

$$\partial_t U_a(t) = -iH_a(t)U_a(t). \tag{2.68}$$

To make the variable dimensionless, we denote the new rescaled time $s = t/T$ ($s \in [0,1]$) with T being the total time, and we have:

$$\partial_s U_a(s) = -iTH_a(s)U_a(s). \tag{2.69}$$

By definition of a perfect adiabatic process, if the system starts in an eigenstate $|\psi_i(0)\rangle$, it will stay in that eigenstate at any time t, such that

$$U_a(s)\,|\psi_i(0)\rangle = e^{i\theta(s)}e^{i\gamma(s)}\,|\psi_i(s)\rangle\,, \tag{2.70}$$

where θ and γ are the phases described in Eq. (2.66). Therefore, an adiabatic unitary U_a preserves the subspace:

$$P(s) = \sum_{i=1}^{d} U_a(s)|\psi_i(0)\rangle\langle\psi_i(0)|U_a^\dagger(s) = U_a(s)P(0)U_a^\dagger(s). \tag{2.71}$$

An important property of the projector $P(s)$ is that:

$$U_a(s)P(0) = P(s)U_a(s). \tag{2.72}$$

We can verify this property by multiplying a starting eigenstate $|\psi_i(0)\rangle$ on both sides in Eq. (2.72):

$$LHS \Rightarrow U_a(s)P(0)\,|\psi_i(0)\rangle = U_a(s)\,|\psi_i(0)\rangle = |\psi_i(s)\rangle\,, \tag{2.73}$$
$$RHS \Rightarrow P(s)U_a(s)\,|\psi_i(0)\rangle = P(s)\,|\psi_i(s)\rangle = |\psi_i(s)\rangle\,. \tag{2.74}$$

We are now interested in how the ideal adiabatic Hamiltonian $H_a(s)$ is related to the real Hamiltonian $H(s)$ and how close they are. We first start with Eq. (2.72):

$$P(s) = U_a(s)P(0)U_a^\dagger(s), \tag{2.75}$$

with $P^\dagger(s) = P(s)$. Taking the time derivative of $P(s)$, combining it with Eq. (2.69):

$$\begin{aligned}\partial_s P(s) &= \partial_s U_a(s)P(0)U_a^\dagger(s) + U_a(s)P(0)\partial_s U_a^\dagger(s) \\ &= -iTH_a(s)U_a(s)P(0)U_a^\dagger(s) + iTU_a(s)P(0)U_a^\dagger(s)H_a(s),\end{aligned} \tag{2.76}$$

that we can rewrite as

$$\partial_s P(s) = iT\,[P(s), H_a(s)]\,. \tag{2.77}$$

It turns out that there exists a Hamiltonian $H_a(s)$ satisfying Eq. (2.77):

$$H_a(s) = H(s) + \frac{i}{T}[\partial_s P(s), P(s)]. \tag{2.78}$$

To evaluate how adiabatic the evolution dictated by the physical Hamiltonian $H(s)$ can be, we use operator norm to characterize the closeness between ideal adiabatic evolution $U_a(s)$ and real evolution $U(s)$ is indicated by the operator norm:

$$F(s) = \|(U(s) - U_a(s))P(0)\|. \tag{2.79}$$

In Ref. [55, 56], *Lemma 1* states that if there exist two bounded functions $X(s)$ and Y(s), satisfying:

$$[\dot{P}(s), P(s)] = [H(s), X(s)] + Y(s), \tag{2.80}$$

then the fidelity $F(s)$ is bounded:

$$F(s) \leq \max_{s\in[0,1]} \left(\frac{2\|X(s)P(s)\| + \|\partial_s(X(s)P(s))P(s)\|}{T} + \|Y(s)P(s)\| \right). \tag{2.81}$$

Eq. (2.81) sets a bound that limits the adiabaticity of real evolution, and a larger duration T means a lower deviation from the ideal adiabatic evolution that a real process can reach.

2.3.3 Effective Hamiltonian in adiabatic theorem

Kato's adiabatic theorem states that in adiabatic evolution, the state can stay in an eigen subspace separated from the complementary subspace by a gap in energy. This motivates the idea of extracting an effective Hamiltonian in a system undergoing an adiabatic process so that it can be approximately modeled as part of the system with only a small deviation from reality. A mathematical theory of how an unbounded Hamiltonian can be described by an effective finite-dimensional Hamiltonian with a cutoff was formulated in Ref. [51]. Here, we give a brief introduction to the formulation. Most of the notations and definitions follow the previous section.

Let's now consider a full Hamiltonian $H(s)$ consisting of two complementary energy eigen subspaces by denoting two projectors P corresponding to the lower energy band. The ideal, perfect adiabatic evolution U_a is generated by H_a:

$$\partial_s U_a(s) = -iTH_a(s)U_a(s), \tag{2.82}$$

and $U_a(0) = I$. Following the theory in Ref. [51], the evolution of the subspace P in the full Hamiltonian $H(s)$ is given by the effective Hamiltonian,

$$H_{\text{eff}}(s) = V_0 U_{\text{eff}}^{\dagger} H(s) U_{\text{eff}} V_0^{\dagger}. \tag{2.83}$$

The operator V_0 denotes basis change from the d-lowest eigenstates of $H(0)$ to the new set of basis $|q_i\rangle$ in the $d-$dimensional Hilbert space:

$$V_0 = \sum_{i=1}^{d} |q_i\rangle\langle\psi_i(0)|. \tag{2.84}$$

The effective unitary U_{eff} in the full Hilbert space is given by:

$$\partial_s U_{\text{eff}}(s) = [P', P]U_{\text{eff}}(s). \tag{2.85}$$

The theory implies that if the system follows an adiabatic path, then the evolution can be generated by an effective Hamiltonian in the low-energy eigensubspace.

2.4 Modeling and simulation

In our experiment, we want to implement qubit reset in a fixed-frequency transmon and tunable coupler-based architecture. We use a subset of a 25-qubit processor of which we consider two transmon qubits ($\mathrm{Q}_0, \mathrm{Q}_1$) coupled capacitively via a tunable coupler C_0 (See Fig. 2.5). Each qubit is also coupled to a readout resonator.

Our goal is to reset Q_0 by moving the coupler frequency such that the excitation in Q_0 is transferred to the coupler. Then, the coupler frequency is shifted to resonate with the readout resonator such that the excitation can leak out of the system. We refer to the steps of this process as Qubit-Coupler SWAP (QC SWAP) and Coupler-Resonator SWAP (CR SWAP).

Here, we mainly focus on the QC SWAP gate where we adiabatically tune the coupler (C_0) frequency close to the qubit (Q_0) frequency such that the population in the qubit can be transferred to the coupler.

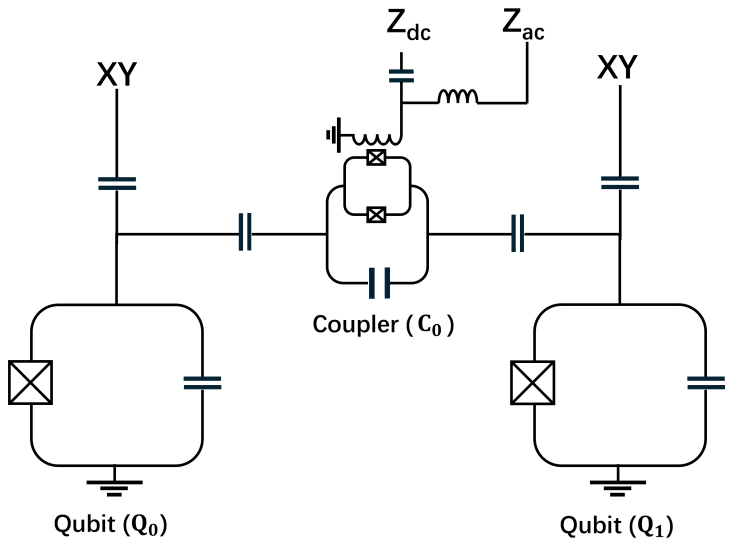

Figure 2.5: Equivalent circuit diagram of a qubit-coupler-qubit model and control lines. For each qubit, the microwave drive is sent through an XY line capacitively coupled to the transmon. The coupler is tuned by a changing external DC and AC flux coupled to the flowing current through the Z line. The readout resonators are omitted in this picture.

2.4.1 System Hamiltonian

We consider a simple model consisting of the transmon qubit Q_0 coupled with the coupler C_0 with a coupling rate g. The qubit (coupler) has resonant frequency ω_q (ω_c) and anharmonicity $\alpha(\beta)$. With these parameters, the Hamiltonian for the QC SWAP step is written as:

$$H = \omega_q a^\dagger a + \frac{\alpha}{2} a^\dagger a^\dagger a a + \omega_c b^\dagger b + \frac{\beta}{2} b^\dagger b^\dagger b b + g(a^\dagger b + a b^\dagger), \tag{2.86}$$

where the ladder operators a and b corresponds to qubit Q_0 and coupler C, respectively. As a toy model, we first neglect the other qubit Q_1, assuming it is far detuned from the rest of the system. To further simplify the model, we can write down the unbounded Hamiltonian in the block-diagonal form:

$$H = \begin{pmatrix} H_{1\times1}^{0-\text{excitation}} & & & \\ & H_{2\times2}^{1-\text{excitation}} & & \\ & & H_{3\times3}^{2-\text{excitation}} & \\ & & & \ddots \end{pmatrix}. \tag{2.87}$$

Each block $H_{(m+1)\times(m+1)}^{m-\text{excitation}}$ is an excitation-conserved Hamiltonian spanned by qubit-coupler composite bare states $\{|n_q n_c\rangle = |n_q\rangle \otimes |n_c\rangle\}_{n_q+n_c=m}$, describing the transition between bare states with the same excitation number connected by the non-diagonal elements. Note that in this model, there is no transition between states with different excitation numbers. Therefore, there is no off-block-diagonal element connecting different blocks in the matrix.

To reset a qubit prepared in $|n_q n_c\rangle = |10\rangle$, we look into the 1-excitation block $H_{qc} = H_{2\times2}^{1-\text{excitation}}$ with basis $|10\rangle$ and $|01\rangle$:

$$\begin{aligned} H_{qc}(t) &= \begin{pmatrix} \omega_q & g \\ g & \omega_c(t) \end{pmatrix} \\ &= \frac{\omega_q + \omega_c(t)}{2} I - \frac{\omega_c(t) - \omega_q}{2}\sigma_z + g\sigma_x \\ &= \frac{\Delta(t)}{2}\sigma_z + g\sigma_x, \end{aligned} \tag{2.88}$$

with $\Delta(t) = \omega_q - \omega_c(t)$ and the Pauli operators σ_z and σ_x:

$$\sigma_z = \begin{pmatrix} 1 & 0 \\ 0 & -1 \end{pmatrix}, \tag{2.89}$$

$$\sigma_x = \begin{pmatrix} 0 & 1 \\ 1 & 0 \end{pmatrix}. \tag{2.90}$$

In $|f\rangle$-state reset, the system is prepared in $|n_q n_c\rangle = |20\rangle$, and the process is modeled in the two-excitation subspace. The Hamiltonian in the Hilbert subspace spanned by the bare basis $|20\rangle$, $|11\rangle$ and $|02\rangle$ reads:

$$\begin{aligned} H(t) &= \begin{pmatrix} 2\omega_q + \alpha & \sqrt{2}g & 0 \\ \sqrt{2}g & \omega_q + \omega_c(t) & \sqrt{2}g \\ 0 & \sqrt{2}g & 2\omega_c(t) + \beta \end{pmatrix} \\ &= (2\omega_q + \alpha)|20\rangle\langle 20| + (\omega_q + \omega_c(t))|11\rangle\langle 11| + (2\omega_c(t) + \beta)|02\rangle\langle 02| + \\ &+ \sqrt{2}g(|20\rangle\langle 11| + |11\rangle\langle 20| + |11\rangle\langle 02| + |02\rangle\langle 11|). \end{aligned} \tag{2.91}$$

We can move into the rotating frame by the transformation $R(t)$ defined as:

$$R(t) = \exp\{-i(2\omega_q + \alpha)[|20\rangle\langle 20| + |11\rangle\langle 11| + |02\rangle\langle 02|]t\}. \tag{2.92}$$

The Hamiltonian in this rotating frame with $R(t)$ is obtained by:

$$\begin{aligned} H(t) &= R^\dagger(t)H(t)R(t) - iR^\dagger(t)\dot{R}(t) \\ &= -(\Delta(t) + \alpha)|11\rangle\langle 11| - (2\Delta(t) + \alpha - \beta)|02\rangle\langle 02| + \\ &+ \sqrt{2}g(|20\rangle\langle 11| + |11\rangle\langle 20| + |11\rangle\langle 02| + |02\rangle\langle 11|). \end{aligned} \tag{2.93}$$

The matrix form of the Hamiltonian in Eq. (2.93) in the Hilbert subspace is:

$$H_{3\text{ls}}(t) = \begin{pmatrix} 0 & \sqrt{2}g & 0 \\ \sqrt{2}g & \Delta(t) & \sqrt{2}g \\ 0 & \sqrt{2}g & \delta(t) \end{pmatrix}, \tag{2.94}$$

where $\Delta(t) = -\Delta_{qc}(t) - \alpha$ and $\delta(t) = -2\Delta_{qc}(t) + \beta - \alpha$.

2.4.2 Local adiabaticity condition for a two-level system

In this section, we review the Roland-Cerf protocol introduced in 2002 [57], which was first designed to help speed up adiabatic quantum computing by considering the energy gap locally and generalizing the original adiabaticity condition. Based on this protocol, many theories and experimental implementations in different platforms have been proposed to accelerate the adiabatic process [58–61]. Here, we follow the key steps in [57] and derive a pulse tailored to perform qubit reset.

The model is assumed to be a simple qubit coupled with a strength g to a tunable coupler. We examine how the qubit state evolves governed by the reset flux pulse based on RC protocol. In the simulation, the system is initialized to $|n_q n_c\rangle = |10\rangle$ and the only tunable control parameter is the qubit-coupler detuning $\Delta_{qc}(t) = \omega_q - \omega_c(t)$. Remember that such a system is well-described by the typical TLS Hamiltonian:

$$H(t) = \frac{\Delta_{qc}(t)}{2}\sigma_z + g\sigma_x. \tag{2.95}$$

For a two-level system, the Hamiltonian $H(s)$ depending on some parameter s in the adiabatic process at every s is:

$$H(s) = (1-s)H_i + sH_f. \tag{2.96}$$

Where $s = s(t) = t/T$ is time-dependent. The Hamiltonian $H(s)$ is constructed by interpolating, linearly in s, between the initial Hamiltonian H_i and the final Hamiltonian H_f linearly with s. The adiabaticity can be guaranteed if the following condition for the evolution time T holds throughout the evolution:

$$T \gg \frac{\max\limits_{0\le s\le 1} |\langle\psi_1(s)|\partial_s H(s)|\psi_0(s)\rangle|}{\min\limits_{0\le s\le 1} |E_1(s) - E_0(s)|^2}, \tag{2.97}$$

where $|\psi_0(s)\rangle$ and $|\psi_1\rangle$ denote the eigenstates of $H(s)$ with their energies $E_0(s)$ and $E_1(s)$. Eq. (2.97) can also be expressed with respect to time t:

$$T \gg \frac{\max\limits_{0\le t\le T} \left|\langle\psi_1(t)|\left(\frac{\partial s}{\partial t}\right)^{-1}\frac{\partial H(t)}{\partial t}|\psi_0(t)\rangle\right|}{\min\limits_{0\le t\le T} |E_1(t) - E_0(t)|^2}, \tag{2.98}$$

since $\partial s/\partial t = 1/T$, Eq. (2.98) becomes:

$$\frac{\max\limits_{0\le t\le T} \left|\langle\psi_1(t)|\frac{\partial H(t)}{\partial t}|\psi_0(t)\rangle\right|}{\min\limits_{0\le t\le T} |E_1(t) - E_0(t)|^2} \ll 1. \tag{2.99}$$

Eq. (2.99) is a global condition, meaning that the LHS in Eq. (2.99) does not change throughout the evolution (time-independent). Intuitively, this inequality can also

be the condition in a very short time interval Δt. For the time interval from t to $t + \Delta t$, the Eq. (2.99) becomes:

$$\frac{\max\limits_{t\leq t'\leq t+\Delta t}\left|\langle\psi_1(t')|\frac{\partial H(t')}{\partial t'}|\psi_0(t')\rangle\right|}{\min\limits_{t\leq t'\leq t+\Delta t}|E_1(t')-E_0(t')|^2}\ll 1. \tag{2.100}$$

If $\Delta t \to 0$, Eq. (2.100) becomes:

$$\left|\langle\psi_1(t)|\frac{\partial H(t)}{\partial t}|\psi_0(t)\rangle\right| \ll |E_1(t)-E_0(t)|^2. \tag{2.101}$$

To perform an adiabatic QC SWAP between qubit and coupler, we need to satisfy the local adiabaticity condition in Eq. (2.101). In the $\Delta t \to 0$ limit, by inserting the qubit-coupler TLS Hamiltonian in Eq. (2.88) into Eq. (2.101), we can obtain the local adiabaticity condition at time t:

$$\left|\frac{\partial \Delta_{qc}}{\partial t}\right| \ll \frac{2|E_1(t)-E_0(t)|^2}{|\langle\psi_1(t)|\sigma_z|\psi_0(t)\rangle|}. \tag{2.102}$$

The instantaneous eigenstates $|\psi_0(t)\rangle$, $|\psi_1(t)\rangle$ and their eigenvalues $E_0(t)$ and $E_1(t)$ can be directly obtained from the TLS Hamiltonian H_{qc} in Eq. (2.88). The instantaneous energy difference is:

$$\Delta E(t) = |E_1(t)-E_0(t)| = \sqrt{\Delta_{qc}^2(t)+4g_{qc}^2}. \tag{2.103}$$

Then the adiabaticity condition for the instantaneous change in $\Delta_{qc}(t)$ is:

$$\left|\frac{\partial \Delta_{qc}(t)}{\partial t}\right| \ll \frac{1}{g_{qc}}(\Delta_{qc}^2(t)+4g_{qc}^2)^{\frac{3}{2}}. \tag{2.104}$$

Appendix A.2 and Appendix A.3 show how we can arrive at Eq. (2.104). The adiabatic reset pulse can be obtained by solving the following differential equation, where we introduced a prefactor γ ranging from 0 to 1:

$$\frac{\partial \Delta_{qc}(t)}{\partial t} = \gamma\frac{1}{g_{qc}}(\Delta_{qc}^2(t)+4g_{qc}^2)^{\frac{3}{2}}. \tag{2.105}$$

Eq. (2.105) can be solved numerically or analytically. To numerically solve Eq. (2.105) at each time step $t_m = m\Delta t$, the corresponding amplitude $\Delta_{qc}(t_m)$ is obtained by:

$$\Delta_{qc}(t_m) = \Delta_{qc}(t_{m-1}) + \gamma\frac{(\Delta_{qc}^2(t_{m-1})+4\bar{g}^2)^{\frac{3}{2}}}{\bar{g}}\Delta t. \tag{2.106}$$

We can also directly solve this differential equation analytically and find an explicit expression of $\Delta_{qc}(t)$:

$$\boxed{\Delta_{qc}(t) = -\frac{8(\gamma\bar{g}t+c)}{\sqrt{1-16(\gamma\bar{g}t)^2-32\gamma\bar{g}ct-16c^2}}}, \tag{2.107}$$

where γ and c are undetermined constants. Notice that we have replaced the device parameter g_{qc} with a tunable pulse parameter controlling the shape of the pulse, $\bar{g}$. If we specify the initial condition $\Delta_{qc}(0) = \Delta_0$ and final condition $\Delta_{qc}(T) = \Delta_T$ with T being the duration of the pulse, then γ and c can be solved:

$$c = -\frac{\Delta_0}{\sqrt{16\Delta_0^2 + 64\bar{g}^2}}, \tag{2.108}$$

$$\gamma = \frac{-4c(\Delta_T^2 + 4\bar{g}^2) - \Delta_T\sqrt{\Delta_T^2 + 4\bar{g}^2)}}{4\bar{g}T(\Delta_T^2 + 4\bar{g}^2)}. \tag{2.109}$$

Typically, the coupler frequency is parked above the qubit frequency and is moved to pass through the qubit frequency, reaching the final point below the qubit to be reset. The prefactor γ controls the time scale of the adiabatic evolution, as shown in Fig. 2.6. This is because a larger γ implies a larger gradient in Eq. (2.106) for each iteration in numerically solving the differential equation.

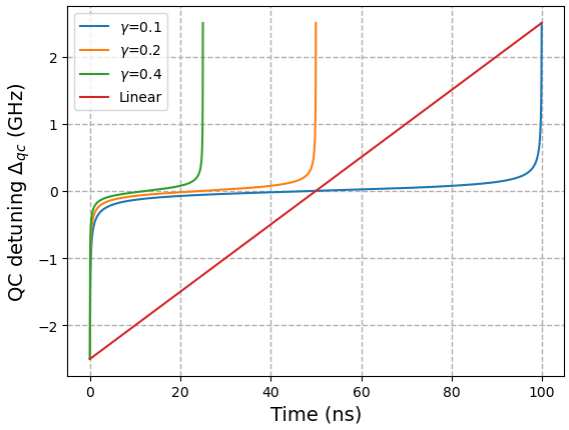

Figure 2.6: QC detuning in the QC swap based on RC protocol with different scaling factors $\gamma = 0.1, 0.2, 0.4$ and a linear pulse for comparison. The coupling rate g_{qc} is 50 MHz and the QC detuning Δ_{qc} is tuned from $-50g_{qc}$ to $50g_{qc}$.

In the $|e\rangle$-state reset, the error of QC SWAP is defined as the population left in all other states than the state $|n_q n_c\rangle = |01\rangle$ that we want to populate:

$$\varepsilon_{|e\rangle} = 1 - |\langle\psi(T)|01\rangle|^2, \tag{2.110}$$

where $|\psi(T)\rangle$ is the final state at the end of the evolution. The RC protocol generally gives low reset error below 1% (see Fig. 2.7). It is evident that compared to a linear flux pulse following the same initial to the final qubit-coupler detuning with the same duration, the local adiabatic condition reduces the reset error greatly, and the pulse duration can be made even shorter without significantly compromising fidelity.

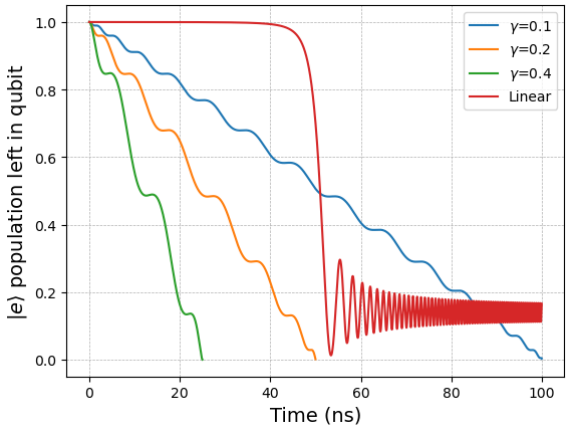

Figure 2.7: Population left in qubit after QC SWAP using the different pulses given in Fig. 2.6.

The adiabaticity can be defined as the overlap between real state $|\psi(t)\rangle$ and the $n-$th eigenstate $|\psi_n(t)\rangle$ of the Hamiltonian $H(t)$ at t, denoted by $\Omega(t)$:

$$\Omega(t) = |\langle\psi(t)|\psi_n(t)\rangle|^2. \tag{2.111}$$

The adiabaticity as a function of time is shown in Fig. 2.8, suggesting that a longer evolution duration (smaller γ) on average leads to more adiabatic evolution with also smaller diabatic oscillation, making it more robust. Physically, the oscillation frequency is the instantaneous energy gap between two eigenstates.

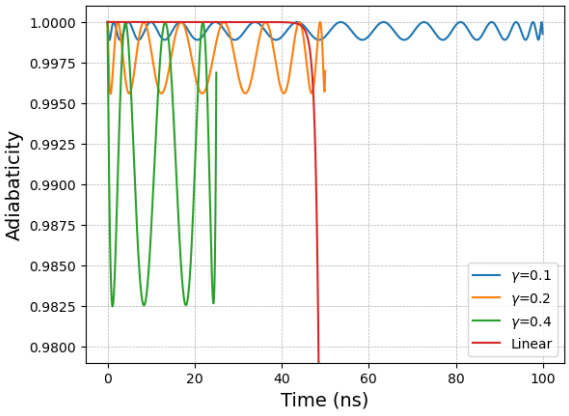

Figure 2.8: Tracking adiabaticity over time for the different pulses in Fig. 2.6 during QC SWAP.

To this point, we have discussed how the scaling factor γ, or duration T, affects adiabatic reset. However, shortcut-to-adiabaticity (STA) can provide a faster and more robust pulse shape. First, we can directly obtain $\Delta_{qc}(t)$ from the analytical form in Eq. (2.107), and by varying g as a pulse parameter, the pulse shape also changes (see Fig. 2.9).

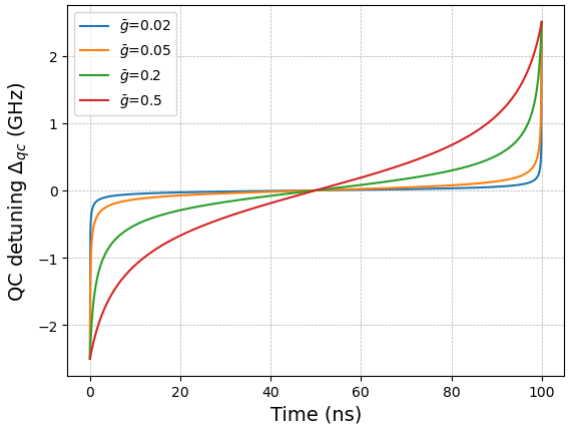

Figure 2.9: Different flux pulses given shape parameters ($\bar{g} = 0.02, 0.05, 0.2, 0.5$ GHz). The shape parameter $\bar{g}$ controls the slope of the pulses.

The evolution indicated by the population in $|e\rangle$-state and adiabaticity are shown in Fig. 2.9. It is worth noting that for $\bar{g} = 0.2$, the state follows a shortcut-to-adiabaticity (STA) path, where the transition to another state occurs amid the evolution but arrives at the desired state at the end of the pulse, yielding better adiabaticity and lower diabatic oscillation error and therefore less reset error.

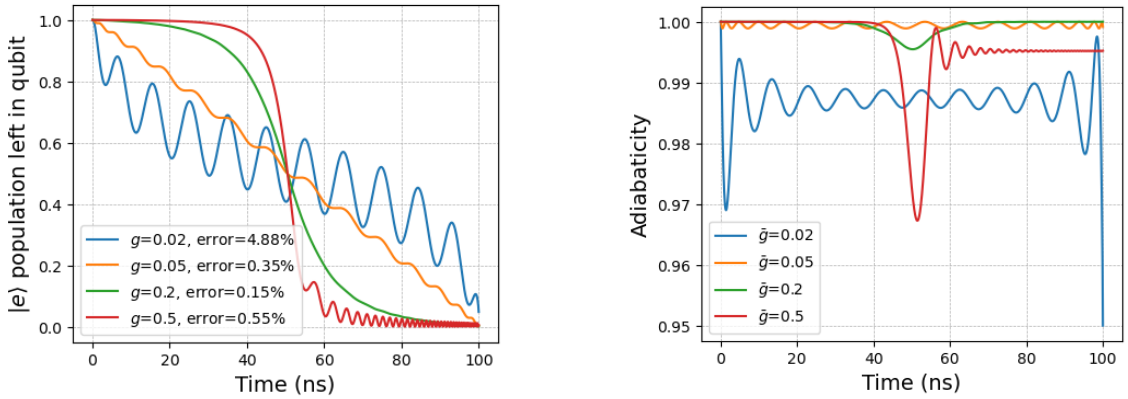

Figure 2.10: Population left in qubit $|e\rangle$ level (left) and adiabaticity over time (right) in $|e\rangle$-state reset using pulses for different shape parameter $\bar{g}$ in Fig. 2.9. The shape parameter controls the adiabaticity, and STA is observed when $\bar{g} = 0.2$.

2.4.3 Local adiabaticity condition for three-level system in $|f\rangle$-state reset

Given the three-level system described by the Hamiltonian mentioned previously in Eq. (2.94):

$$H_{3\text{ls}}(t) = \begin{pmatrix} 0 & \sqrt{2}g & 0 \\ \sqrt{2}g & \Delta(t) & \sqrt{2}g \\ 0 & \sqrt{2}g & \delta(t) \end{pmatrix}, \tag{2.112}$$

an adiabatic path for $\Delta_{qc}(t) = -\Delta(t) - \alpha$ can be found using a method similar to the one used in Sec. 2.4.2 for the $|e\rangle$-state reset in the previous section. It is straightforward to apply the instantaneous adiabaticity condition in Eq. (2.101) with the undetermined factor γ

$$\left|\langle\psi_1(t)|\frac{\partial H_{3\text{ls}}(t)}{\partial t}|\psi_0(t)\rangle\right| = \gamma|E_1(t) - E_0(t)|^2, \tag{2.113}$$

arriving at the differential equation (see Appendix A.4):

$$\frac{\partial\Delta_{qc}}{\partial t} = \gamma\frac{(E_1(t) - E_0(t))^2}{|\langle\psi_1(t)|A|\psi_0(t)\rangle|}, \tag{2.114}$$

where A is a three-by-three matrix

$$A = \begin{pmatrix} 0 & 0 & 0 \\ 0 & 1 & 0 \\ 0 & 0 & 2 \end{pmatrix}. \tag{2.115}$$

We use numerical methods to solve Eq. (2.114) iteratively for each time step Δt, and specify the scaling factor γ and boundary conditions

$$\Delta_{qc}(t_{m+1}) = \Delta_{qc}(t_m) + \gamma\frac{(E_1(t_m) - E_0(t_m))^2}{|\langle\psi_1(t_m)|A|\psi_0(t_m)\rangle|}\Delta t, \tag{2.116}$$

where $t_m = m\Delta t$ with m is a positive integer. The two lowest eigenstates $|\psi_0(t_m)\rangle$ and $|\psi_1(t_m)\rangle$ with eigenvalues $E_0(t_m)$ and $E_1(t_m)$ are computed by numerically diagonalizing $H_{3\text{ls}}(t;\bar{g})$ where $g \to \bar{g}$ in Eq. (2.112).

Here, we illustrate the qubit-coupler detuning trajectories (Fig. 2.11(left)) and corresponding adiabaticity Fig. 2.11(right) over time of an adiabatic pulse, an STA pulse (by solving Eq. (2.114)) and a linear pulse for comparison. The simulation results where the system starts with state $|n_q n_c\rangle = |20\rangle$ are shown in Fig. 2.12, showing that the STA perfectly resets $|f\rangle$-state level within a shorter time with an error rate (population left in qubit) below 1%, while the leakage to $|11\rangle$ is around 2.13%.

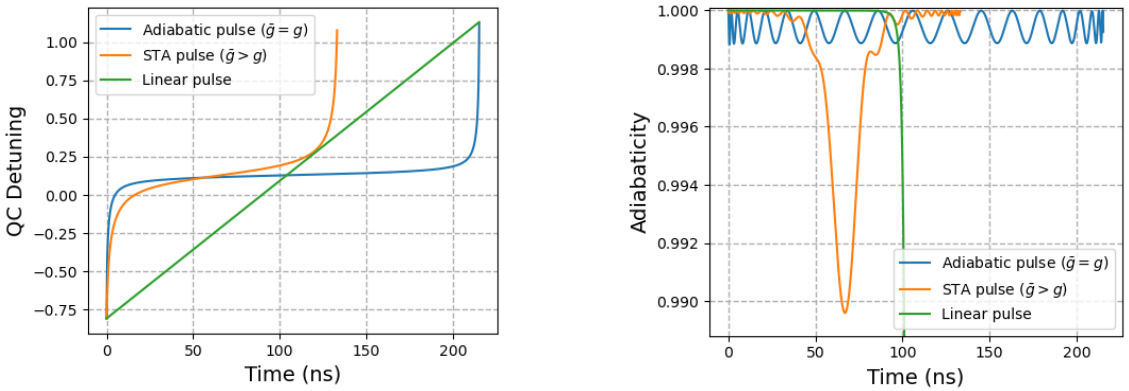

Figure 2.11: (Left) Adiabatic, STA and linear pulses and (right) corresponding adiabaticity over time in $|f\rangle$ −state reset during evolution. The adiabatic pulse is based on RC protocol and is numerically obtained from Eq. (2.114). The qubit frequency f_q is 5.176 GHz with anharmonicity $\alpha = -256$ MHz, and the coupler is tuned from $f_0 = 5.989$ GHz to $f_t = 4.109$ GHz. For adiabatic pulse the shape parameter $\bar{g}$ is 47 MHz and γ is 0.1; For STA pulse $\bar{g}$ is 100 MHz and γ is 0.06. From the result, it is clear that the STA pulse can accelerate the adiabatic process while ensuring relatively good adiabaticity when compared to the adiabatic and linear pulses.

The shortcut in adiabaticity can be observed when $\bar{g} > g$, indicating that the eigensubspace of $H_{3\text{ls}}$ with projection onto the lowest two eigenstates can be treated as a two-level system, provided that for both adiabatic and STA evolution, the leakage to the third eigenstate can be negligible and only the lowest two levels are involved.

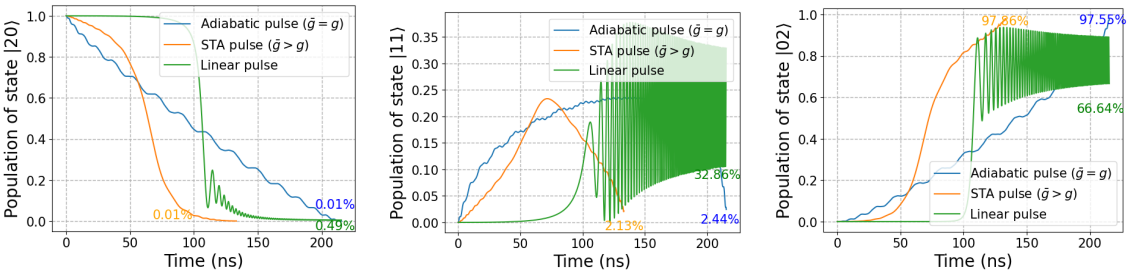

Figure 2.12: Population in states (left) $|20\rangle$, (middle) $|11\rangle$ and (right) $|02\rangle$ during evolution using different pulses in Fig. 2.11. For linear pulse, the leakage and diabatic oscillation in $|11\rangle$ and $|02\rangle$ hinder the performance and robustness of QC SWAP gate. Using STA, we can ensure faster gate operation and better reset fidelity.

The problem with this numerical method is that the eigenstates $|\psi_0(t_m)\rangle$, $|\psi_1(t_m)\rangle$ and their eigenenergies $E_0(t_m)$, $E_1(t_m)$ are numerically obtained from $H_{3\text{ls}}(t_m; \bar{g})$, which requires a lot of time and computation resources and therefore not applicable in the lab. Hence, it is desired to obtain an analytical expression for $|f\rangle$-state reset.

2.4.4 Effective TLS Hamiltonian in $|f\rangle$-state reset

In adiabatic qubit reset, the coupler frequency is first brought close to the avoided level-crossing and passes through it adiabatically. Therefore, many block-diagonalization techniques based on perturbation theory no longer work in this non-perturbative regime where the difference between diagonal elements is much smaller than the off-diagonal elements.

To address this problem, an analytical method called non-perturbative analytical diagonalization (NPAD) [62] is used in extracting effective TLS Hamiltonian. In diagonalization, NPAD doesn't require any perturbation assumption and can give convergent results with more iterations. Here, we show how NPAD is done in our analysis to derive an effective Hamiltonian. In each iteration, the off-diagonal element entries (i, j) and (j, i) connecting diagonal element (i, i) and (j, j) are eliminated by a Givens rotation $U(i, j)$:

$$U(i,j) = \begin{pmatrix} 1 & & & & & & \\ & \ddots & & & & & \\ & & c_{ii} & \cdots & s_{ij} & & \\ & & \vdots & & \vdots & & \\ & & s_{ji} & \cdots & c_{jj} & & \\ & & & & & \ddots & \\ & & & & & & 1 \end{pmatrix}, \tag{2.117}$$

where the subscript denotes the entry position and $s_{ij} = s_{ji}$ and $c_{ii} = c_{jj}$:

$$c_{ii} = c_{jj} = \cos(\theta_{ij}/2), \tag{2.118}$$
$$s_{ij} = s_{ji} = \sin(\theta ij/2). \tag{2.119}$$

The angle θ_{ij} is obtained by:

$$\theta_{ij} = \arctan\left(\frac{H_{ij}}{(H_{ii} - H_{jj})/2}\right), \tag{2.120}$$

with H_{ij}, H_{ii} and H_{jj} being the Hamiltonian elements.

Motivated by the simulation results in Fig. 2.11 and Fig. 2.12 the pulse in Fig. 2.11(left) and the simulation result in Fig. 2.12, we can extract an effective TLS Hamiltonian from the typical three-level Hamiltonian H_{3ls} that we want to block-diagonalize:

$$H_{\text{3ls}} = \begin{pmatrix} 2\omega_q + \alpha & g & 0 \\ g & \omega_q + \omega_c & g \\ 0 & g & 2\omega_c \end{pmatrix}, \tag{2.121}$$

where the coupling $\sqrt{2}g$ is replaced by g for simplicity and the bases are the uncoupled states $|qc\rangle = |20\rangle$, $|11\rangle$ and $|02\rangle$. We'll first look at the simple toy model where

the qubit anharmonicity α is 0. By adding an energy offset $-(3\omega_q + \omega_c)/2$ to the diagonal, H_0 becomes:

$$H_0 = \begin{pmatrix} \Delta & g & 0 \\ g & -\Delta & g \\ 0 & g & -3\Delta \end{pmatrix}, \tag{2.122}$$

where $\Delta = (\omega_q - \omega_c)/2$. Each diagonal element as a function of Δ of H_0 is plotted in Fig. 2.13.

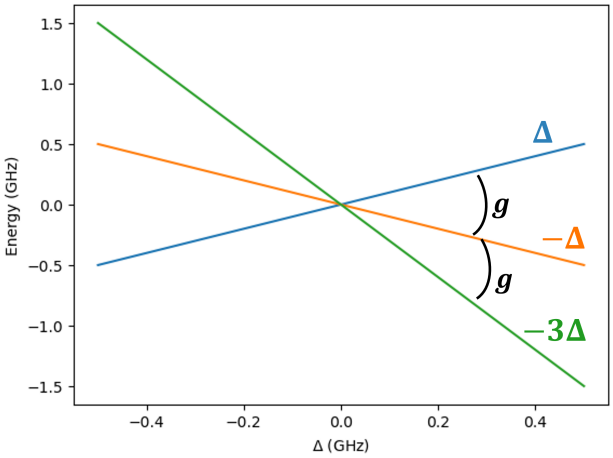

Figure 2.13: The energy diagram of the diagonal elements in H_0. The energies of the uncoupled states are $E_1 = \Delta$, $E_2 = -\Delta$ and $E_3 = -3\Delta$. The coupling rate g denotes coupling between E_1 and E_2, E_2 and E_3.

The first Givens rotation is to uncouple these two states with energies $E_1 = \Delta$ and $E_2 = -\Delta$ by Givens rotation $U^{(1)} = U^{(1)}(0,1)$ transforming H_0 into $H_1 = U^{(1)} H_0 U^{(1)\dagger}$:

$$H_1 = \begin{pmatrix} \frac{|\Delta|\sqrt{\Delta^2+g^2}}{\Delta} & 0 & g\sin\left(\frac{\arctan(g/\Delta)}{2}\right) \\ 0 & -\frac{|\Delta|\sqrt{\Delta^2+g^2}}{\Delta} & g\cos\left(\frac{\arctan g/\Delta}{2}\right) \\ g\sin\left(\frac{\arctan(g/\Delta)}{2}\right) & g\cos\left(\frac{\arctan g/\Delta}{2}\right) & -3\Delta \end{pmatrix}. \tag{2.123}$$

The new energies of the uncoupled diagonal elements in H_1 are $E_1^{(1)} = \pm\sqrt{\Delta^2 + g^2}$ and $E_2^{(1)} = \mp\sqrt{\Delta^2 + g^2}$, $E_3^{(1)} = -3\Delta$ when $\Delta > 0$ ($\Delta < 0$). Consider the regime where $\Delta > 0$, the new coupling rate between $E_2^{(1)}$ and $E_3^{(1)}$ is $c_1 g$ where $c_1 = \cos(\arctan(g/\Delta)/2)$.

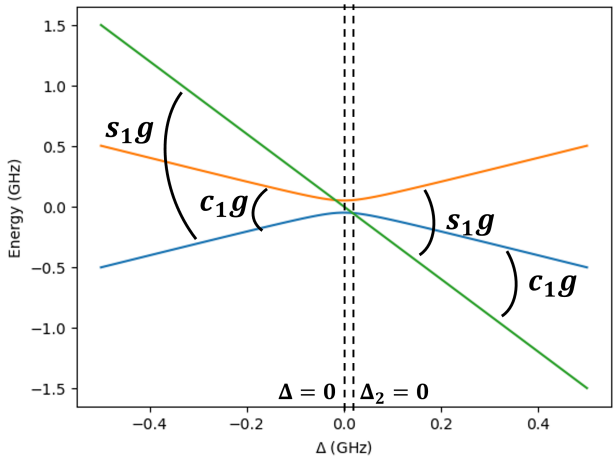

Figure 2.14: The energy diagram of the diagonal elements in H_1 obtained after the first Givens rotation in NPAD.

In the second Givens rotation, we'll remove the coupling between $E_2^{(1)} = -\sqrt{\Delta^2 + g^2}$ and $E_3^{(1)} = -3\Delta$ when $\Delta > 0$. After applying the second rotation $U^{(2)}$, the new Hamiltonian $H_2 = U^{(2)} H_1 U^{(2)^\dagger}$ for $\Delta > 0$ reads:

$$H_2 = \begin{pmatrix} \delta_2 & s_1 s_2 g & s_1 c_2 g \\ s_1 s_2 g & \frac{|\Delta_2|\sqrt{\Delta_2^2 + c_1^2 g^2}}{\Delta_2} & 0 \\ s_1 c_2 g & 0 & -\frac{|\Delta_2|\sqrt{\Delta_2^2 + c_1^2 g^2}}{\Delta_2} \end{pmatrix}, \tag{2.124}$$

where

$$\Delta_2 = \frac{3\Delta - \sqrt{\Delta^2 + g^2}}{2}, \tag{2.125}$$

$$\delta_2 = E_1^{(1)} - \frac{E_2^{(1)} + E_3^{(1)}}{2}, \tag{2.126}$$

$$s_2 = \sin\left(\arctan\left(c_1 g / \Delta_2\right)/2\right), \tag{2.127}$$

$$c_2 = \cos\left(\arctan\left(c_1 g / \Delta_2\right)/2\right). \tag{2.128}$$

The new energies $E_1^{(2)} = H_{2_{0,0}}$, $E_2^{(2)} = H_{2_{1,1}}$ and $E_3^{(2)} = H_{2_{2,2}}$ along the diagonal in H_2 are shown in Fig. 2.15.

From the result in Fig. 2.15, we can see that the lowest state has no level crossing with the other two states in energy. We then need a third rotation to uncouple $E_1^{(2)}$ and $E_2^{(2)}$ when $\Delta_2 < 0$, arriving at the final Hamiltonian $H_3 = U^{(3)} H_2 U^{(3)^\dagger}$:

$$H_3 = \begin{pmatrix} \frac{|\Delta_3|\sqrt{\Delta_3^2 + s_1^2 c_2^2 g^2}}{\Delta_3} & s_1 s_2 c_3 g & 0 \\ s_1 s_2 c_3 g & -\frac{\delta_2}{2} - \frac{3\sqrt{\Delta_2^2 + c_1^2 g^2}}{2} & s_1 s_2 s_3 g \\ 0 & s_1 s_2 s_3 g & -\frac{|\Delta_3|\sqrt{\Delta_3^2 + s_1^2 c_2^2 g^2}}{\Delta_3} \end{pmatrix}, \tag{2.129}$$

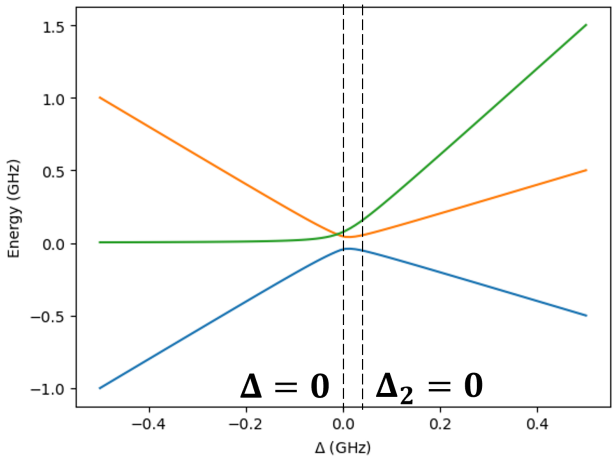

Figure 2.15: The energy diagram of the diagonal elements in H_2 obtained after the second Givens rotation in NPAD.

where

$$\Delta_3 = E_1^{(2)} - (E_1^{(2)} + E_3^{(2)})/2, \tag{2.130}$$

$$s_3 = -\sin\left(\arctan\left(s_1 c_2 g/\Delta_3\right)/2\right), \tag{2.131}$$

$$c_3 = \cos\left(\arctan\left(s_1 c_2 g/\Delta_3\right)/2\right). \tag{2.132}$$

The analytical form of energies computed from NPAD is the diagonal elements in H_3 after three Givens rotations, denoted by $E_1^{(3)}$, $E_2^{(3)}$ and $E_3^{(3)}$. We can plot the lowest two energies $E_1^{(3)}(\Delta)$ and $E_2^{(3)}(\Delta)$ from $\Delta = -10g$ to $\Delta = +10g$ and make comparison with the exact eigenvalues of H_3 (Fig. 2.16).

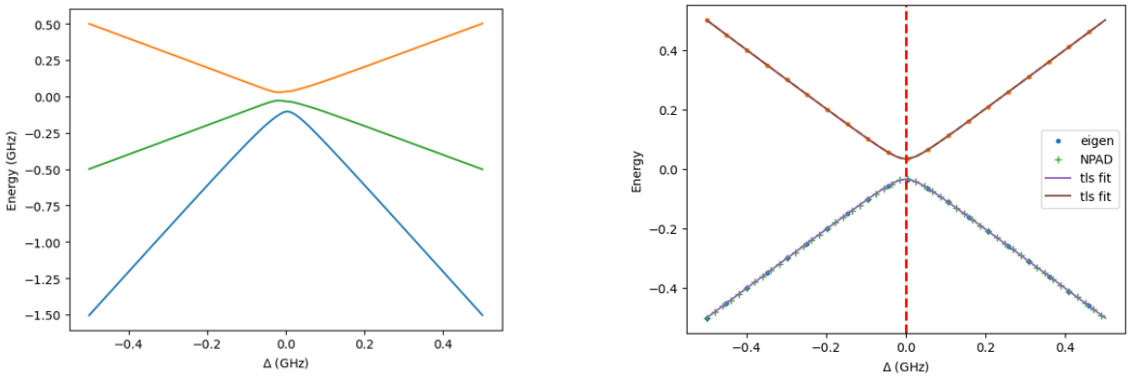

Figure 2.16: The energy diagram using NPAD after three iterations (left) and the rescaled energies of the lowest two energies (right). It is clear that even with only three rotations, the diagonal elements in the transformed Hamiltonian H_3 are very close to the exact eigenvalues. The result also indicates that for zero anharmonicity, the subspace of the three-by-three Hamiltonian H_0 is an approximate TLS Hamiltonian.

By fitting the points with the TLS energies $E_{\mathrm{TLS}} = \pm\sqrt{\Delta^2 + g_{\mathrm{eff}}^2}$, we can see that the eigen subspace in H_3 is approximately a TLS system. To extract the effective

coupling rate g_{eff} in the effective Hamiltonian, we can directly insert $\Delta = 0$ into the analytical expression $g_{\text{eff}} = \frac{E_2^{(3)}(0) - E_1^{(3)}(0)}{2}$ and the effective coupling rate is:

$$g_{\text{eff}} \approx 0.68g. \tag{2.133}$$

Therefore, we can conclude that the effective Hamiltonian for $|f\rangle$-state reset is:

$$H_{\text{eff}} = \begin{pmatrix} \Delta & 0.68\sqrt{2}g_{qc} \\ 0.68\sqrt{2}g_{qc} & -\Delta \end{pmatrix}, \tag{2.134}$$

with $\Delta = (\omega_q - \omega_c)/2$.

Now we'll look at the situation where qubit anharmonicity is not zero. Starting from the original Hamiltonian in Eq. (2.121), the energy is shifted by $-(2\omega_q + 2\omega_c + \alpha)/2$, the Hamiltonian H_0 to be block-diagonalized is:

$$H_0 = \begin{pmatrix} \Delta & 0 & g \\ 0 & -\Delta & g \\ g & g & \delta \end{pmatrix}, \tag{2.135}$$

where $\Delta = \omega_q - \omega_c + \alpha/2$ and $\delta = -\alpha/2$.

As Δ is close to 0, H_0 falls into a weak perturbative regime where the energy difference between the diagonal elements is larger than the inter-block off-diagonal coupling g:

$$\frac{|\Delta - \delta|}{g} > 1. \tag{2.136}$$

Then, this can be seen as an approximate Λ-system, where bare states $|20\rangle$ and $|02\rangle$ indirectly interact with each other through coupling to a far-detuned state $|11\rangle$ at coupling rate g.

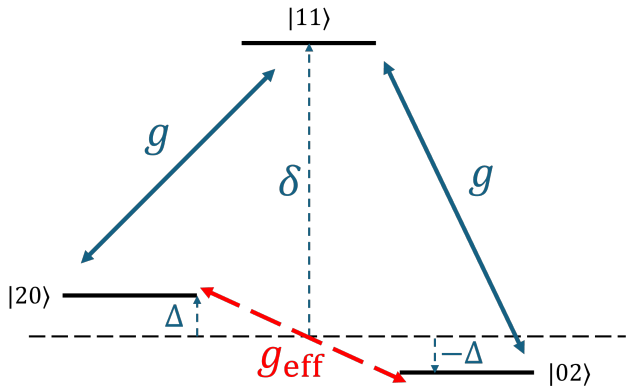

Figure 2.17: Energy diagram of an approximate Λ-system. Bare states $|20\rangle$ and $|02\rangle$ interact with each other via $|11\rangle$.

In the case of $|f\rangle$-state reset, we consider the effective coupling rate g_{eff} between these two states in an effective TLS system by performing a Schrieffer–Wolff transformation (SWT), following the work in Ref. [63–67]. The desired block-diagonalized

Hamiltonian H_{bd} is generated by a transformation $U_{\text{SW}} = e^S$ defined by a generator S:

$$H_{\text{bd}} = e^S H_0 e^{-S} = H_0 + [S, H_0] + \frac{1}{2!}[S, [S, H_0]] + \cdots . \tag{2.137}$$

This expansion can be rewritten by replacing $H_0 = H_{\text{diag}} + H_{\text{ib}}$ with its block diagonalized matrix $H_{\text{diag}} = \text{diag}(H_0)$ and inter-block coupling matrix $H_{\text{ib}} = H_0 - H_{\text{diag}}$ to the second order:

$$H_{\text{swt}} = H_{\text{diag}} + \frac{1}{2}[S, H_{\text{ib}}], \tag{2.138}$$

by imposing this condition:

$$H_{\text{ib}} = -[S, H_{\text{diag}}]. \tag{2.139}$$

The solution for the generator S to Eq. (2.139) is found to be:

$$S_{ij} = \frac{(H_{\text{ib}})_{ij}}{(H_{\text{diag}})_{ii} - (H_{\text{diag}})_{jj}} \text{ when } (H_{\text{ib}})_{ij} \neq 0. \tag{2.140}$$

Therefore, the inter-coupling elements connecting subspaces are eliminated by substituting Eq. (2.140) into Eq. (2.138):

$$H_{\text{swt}} = \begin{pmatrix} \Delta + \frac{g^2}{\Delta - \delta} & \frac{\delta}{(\Delta+\delta)(\Delta-\delta)} g^2 & 0 \\ \frac{\delta}{(\Delta+\delta)(\Delta-\delta)} g^2 & -\Delta - \frac{g^2}{\Delta+\delta} & 0 \\ 0 & 0 & \delta - \frac{2\delta}{(\Delta+\delta)(\Delta-\delta)} g^2 \end{pmatrix}. \tag{2.141}$$

From Eq. (2.138), the effective Hamiltonian $H_{\text{eff,swt}}$ for TLS reads:

$$H_{\text{eff,swt}} = \begin{pmatrix} \Delta + \frac{\Delta g^2}{\Delta^2 - \delta^2} & \frac{\delta}{\Delta^2 - \delta^2} g^2 \\ \frac{\delta}{\Delta^2 - \delta^2} g^2 & -\Delta - \frac{\Delta g^2}{\Delta^2 - \delta^2} \end{pmatrix}, \tag{2.142}$$

which can be further simplified in the regime where $\left|\frac{\Delta}{\delta}\right| \ll 1$:

$$\boxed{H_{\text{eff,swt}} \approx \begin{pmatrix} \left(1 - \frac{g^2}{\delta^2}\right) \Delta & -\frac{g^2}{\delta} \\ -\frac{g^2}{\delta} & -\left(1 - \frac{g^2}{\delta^2}\right) \Delta \end{pmatrix}}, \tag{2.143}$$

with effective detuning $\Delta_{\text{eff}} = (1 - g^2/\delta^2)\Delta$ and effective coupling $g_{\text{eff}} = -g^2/\delta$.

We can also construct an effective TLS Hamiltonian by NPAD, with only two successive Givens rotations to eliminate the interblock, off-diagonal element in Eq. (2.135) one at a time, giving the transformed Hamiltonian:

$$H_{\text{npad}} = \begin{pmatrix} \frac{3\Delta_1}{2} + \delta - \frac{3\sqrt{g^2 + \Delta_1^2}}{2} & s_1 c_2 g & s_1 s_2 g \\ s_1 c_2 g & -\sqrt{\Delta_2^2 + c_1^2 g^2} & 0 \\ s_1 s_2 g & 0 & \sqrt{\Delta_2^2 + c_1^2 g^2} \end{pmatrix}. \tag{2.144}$$

The obtained effective Hamiltonian reads:

$$H_{\text{eff,npad}} = \begin{pmatrix} \Delta_3 & s_1 c_2 g \\ s_1 c_2 g & -\Delta_3, \end{pmatrix} \tag{2.145}$$

where all the notations in Eq. (2.145) are:

$$s_1 = \sin\left(\frac{\arctan(\frac{g}{\Delta_1})}{2}\right), \tag{2.146}$$

$$c_1 = \cos\left(\frac{\arctan(\frac{g}{\Delta_1})}{2}\right), \tag{2.147}$$

$$c_2 = \cos\left(\frac{\arctan(\frac{c_1 g}{\Delta_2})}{2}\right), \tag{2.148}$$

$$\Delta_1 = \frac{\Delta}{2} - \frac{\delta}{2}, \tag{2.149}$$

$$\Delta_2 = \frac{\sqrt{\Delta_1^2 + g^2}}{2} + \frac{3\Delta_1 + 2\delta}{2}, \tag{2.150}$$

$$\Delta_3 = \frac{3\Delta_1 + 2\delta + 2\sqrt{\Delta_2^2 + c_1^2 g^2} - 3\sqrt{\Delta_1^2 + g^2}}{4}. \tag{2.151}$$

Since Δ_3 and $s_1 c_2 g$ are functions of Δ, we can approximate all entries in Eq. (2.145) by expanding them to only the first order of Taylor's series, in the regime where $\Delta \ll g, \delta$:

$$\boxed{H_{\text{eff,npad}} \approx \begin{pmatrix} \chi\Delta & \chi g_{\text{eff}} \\ \chi g_{\text{eff}} & -\chi\Delta \end{pmatrix},} \tag{2.152}$$

where the effective coupling g_{eff} is a function of g and δ, and χ is a dimensionless factor. Appendix A.5 presents how to arrive at the effective Hamiltonian in Eq. (2.152) using NPAD in detail. To validate how well SWT and NPAD approximate the system, we can compute the eigenenergies of effective Hamiltonians $H_{\text{eff,swt}}$ (Eq. (2.143)) and $H_{\text{eff,npad}}$ (Eq. (2.145)), compared with the two lowest eigenenergies of H_0 (Eq. (2.135)), shown in Fig. 2.18.

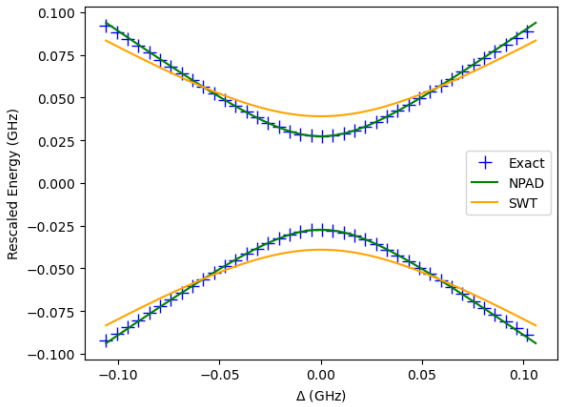

Figure 2.18: Eigenenergies of the effective Hamiltonian using NPAD and SWT, compared with the exact eigenvalues near avoided crossing. Since it's not a strong perturbative system, NPAD is a better approximation over SWT.

After obtaining the effective Hamiltonian in the subspace, the RC protocol-based trajectories of detuning Δ can be solved directly given the differential equation Eq. (2.107) for a TLS.

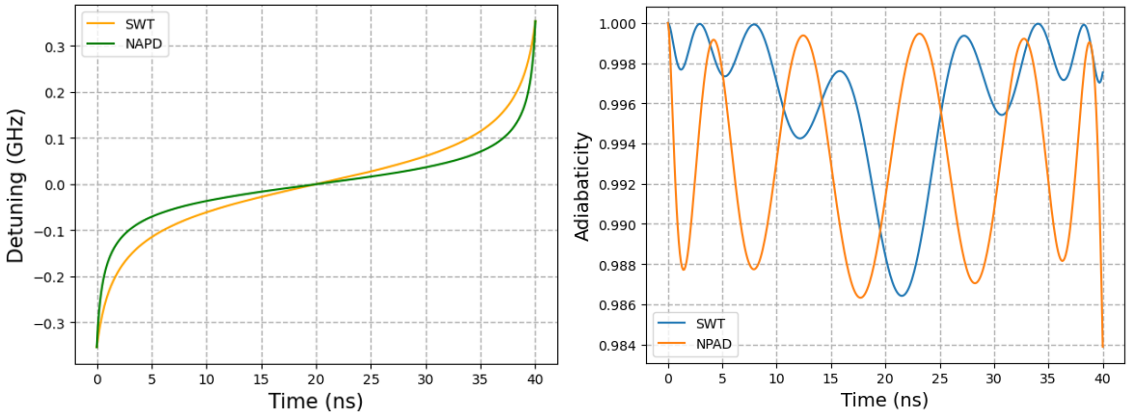

Figure 2.19: Trajectories based on RC protocol and effective Hamiltonians using SWT and NAPD (left) and the corresponding adiabaticity during the evolution (right). The adiabatic path starts from $\Delta = -5g$ to $\Delta = +5g$ in 40 nanoseconds, where $g = 50$ MHz.

The trajectories and adiabaticity over time are plotted in Fig. 2.19. The result suggests that even though NPAD is a better method to extract the TLS Hamiltonian near the avoided crossing regime than SWT, both can be used to design an adiabatic pulse.

2.4.5 Effective Hamiltonian and RC-protocol

For a system whose evolution is governed by a Hamiltonian $H(t)$, the local condition based on the RC-protocol is given by Eq. (2.101) for two adjacent eigenstates $|\psi_{j,k}\rangle$ and energies $E_{j,k}$:

$$\left|\langle\psi_j(t)|\frac{\partial H(t)}{\partial t}|\psi_k(t)\rangle\right| \ll |E_j(t) - E_k(t)|^2. \tag{2.153}$$

Any transformation on $H(t)$ is denoted by $D(t)$, the LHS in Eq. (2.154) can be rewritten:

$$\left|\langle\psi_j(t)|D^\dagger(t)D(t)|\frac{\partial H(t)}{\partial t}|D^\dagger(t)D(t)|\psi_k(t)\rangle\right| \ll |E_j(t) - E_k(t)|^2. \tag{2.154}$$

In the previous sections, the Hamiltonian obtained by block diagonalization is $\tilde{H} = DHD^\dagger$, and the condition used in deriving adiabatic evolution given effective Hamiltonian $\tilde{H}$ is

$$\left|\langle\tilde{\psi}_j(t)|\frac{\partial \tilde{H}(t)}{\partial t}|\tilde{\psi}_k(t)\rangle\right| \ll |E_j(t) - E_k(t)|^2. \tag{2.155}$$

The time derivative of the effective Hamiltonian in Eq. (2.155) can be expanded, and the LHS is

$$\left|\langle\tilde{\psi}_j|\dot{\tilde{H}}|\tilde{\psi}_k\rangle\right| = \left|\left\langle\tilde{\psi}_j\right| D\dot{H}D^\dagger + \dot{D}HD^\dagger + DH\dot{D}^\dagger \left|\tilde{\psi}_k\right\rangle\right|. \tag{2.156}$$

From Eq. (2.156), we arrive at the following inequality:

$$\left|\langle\tilde{\psi}_j|\dot{\tilde{H}}|\tilde{\psi}_k\rangle\right| < \left|\left\langle\tilde{\psi}_j\right| D\dot{H}D^\dagger \left|\tilde{\psi}_k\right\rangle\right| + \left|\left\langle\tilde{\psi}_j\right| \dot{D}HD^\dagger \left|\tilde{\psi}_k\right\rangle\right| + \left|\left\langle\tilde{\psi}_j\right| DH\dot{D}^\dagger \left|\tilde{\psi}_k\right\rangle\right|. \tag{2.157}$$

Therefore, from Eq. (2.154), Eq. (2.155) and Eq. (2.157), we can see that a good block diagonalization $D(t)$ implies that the last two terms in Eq. (2.157) should be as small as possible such that

$$\left|\langle\tilde{\psi}_j|\dot{\tilde{H}}|\tilde{\psi}_k\rangle\right| \approx \left|\langle\tilde{\psi}_j|D\dot{H}D^\dagger|\tilde{\psi}_k\rangle\right|. \tag{2.158}$$

As discussed above, we can see that a possible extended work is to find a better transformation $D(t)$ such that the approximation in Eq. (2.158) is valid in our effective Hamiltonian model.

3

Method

3.1 Chip layout

In the experiment, all components in the quantum processor are integrated into a flip-chip module featuring two separate chips: a quantum chip (Q-chip) and a control chip (C-chip) bonded together [18]. The Q-chip hosts all the transmon qubits and the couplers. All 25 qubits are placed in a layout of 5×5 grid. For each transmon qubit, the coupling to any nearest-neighbor qubit is mediated by a flux-tunable coupler (Fig. 3.1).

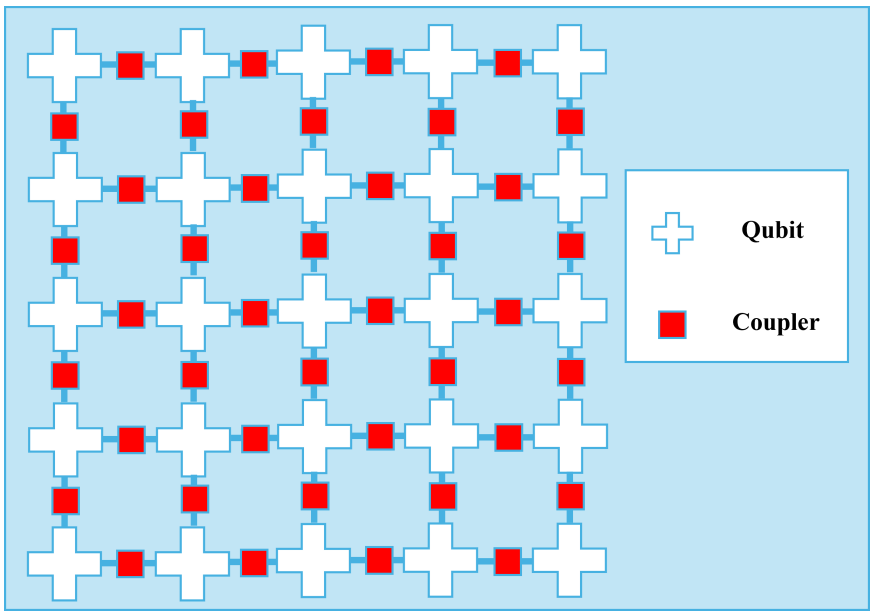

Figure 3.1: Simplified schematics representing the layout of the 25-qubit chip. The 25 qubits are arranged in a 5×5 array on the chip. Each qubit is coupled with all other nearest-neighbor qubits via tunable couplers.

All other components, including the readout resonators, feedlines, Z lines, and XY lines, are placed on the C-chip. The schematic of a pair of qubits (Q_0, Q_1) coupled with the coupler C_0 used in this experiment is shown in Fig. 3.2.

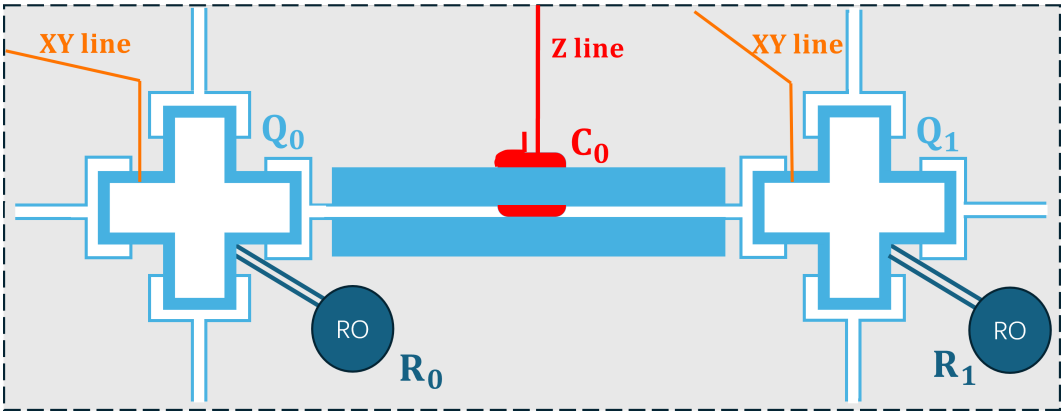

Figure 3.2: Schematic of a subset of the 25-qubit chip in Fig. 3.1. The sample is fabricated using the flip-chip technique. The dedicated readout resonators R_0 and R_1 and Z line are located on the control chip. The qubits Q_0 and Q_1 are driven by the microwave sent through XY lines.

For each qubit, the XY line controls the X and Y gates by supplying microwave drives, and the Z line tunes the coupler frequency by changing the current running through the Z loop. The magnetic flux threading the Z loop on the C-chip couples the flux in the SQUID of the coupler [68]. In the QC SWAP gate, the frequency of C_0 is adiabatically tuned from above Q_0 to a position between Q_0 and Q_1, facilitating the transfer of excitation from Q_0 to C_0 at the cost of leakage to Q_1. After QC SWAP, C_0 is tuned close to R_0 so that excitation in C_0 is swapped to R_0 followed by dissipation into environment. This coupler-resonator excitation swap is ensured by direct and indirect coupling between C_0 and R_0.

3.2 Control setup

In the fixed-frequency qubit and tunable coupler architecture, there are two types of control: microwave drive for qubit gate operation and flux bias for coupler tuning. For qubit gate control, the microwave drive is sent through an XY-line, which is capacitively coupled to the target transmon qubit. The current in the Z line is supplied by a DC source and an AC source, and the signals are combined using a bias tee.

In our experiment, the microwave drives are produced by a QCM-RF module (QBLOX instrument) integrating local oscillators (LO), arbitrary waveform generator (AWG), and IQ mixers. The schematic, as shown in Fig. 3.3, illustrates a simplified schematic explaining how a pulse is generated:
As our baseband signals, the pulses coming from AWG carry information about the pulse envelope and the rotation axis for qubit control on the Bloch sphere. The signals V_I and V_Q transmitted to the IQ mixer through I and Q channels are:

$$V_I(t) = A_I(t)\cos\left(\omega_{\mathrm{IF}}t + \phi_I\right), \tag{3.1}$$

$$V_Q(t) = A_Q(t)\sin\left(\omega_{\mathrm{IF}}t + \phi_Q\right), \tag{3.2}$$

with $A_{I/Q}$, ω_{IF}, $\phi_{I/Q}$ denoting pulse envelope, intermediate frequency, signal phase. The I/Q signal is then mixed with the I/Q component of incoming carrier signal

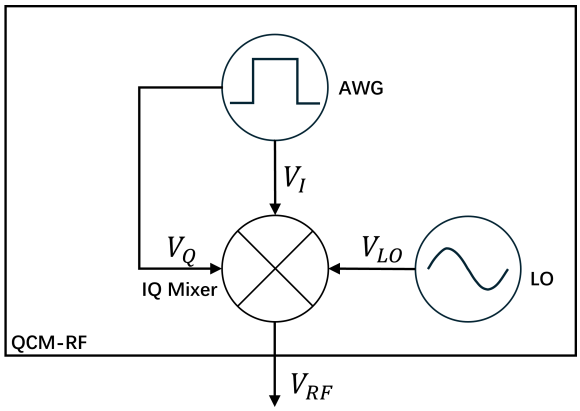

Figure 3.3: Simplified schematics of one output in a QBLOX QCM-RF, featuring an AWG, a LO, and an IQ mixer.

V_{LO} with high frequency ω_{LO} from the LO,

$$V_{\mathrm{LO}}(t) = A_{\mathrm{LO}}(t)\cos\left(\omega_{\mathrm{LO}}t + \phi_{\mathrm{LO}}\right) \tag{3.3}$$

and converted to high-frequency signals at the output port at $\omega_{\mathrm{RF}} = \omega_{\mathrm{LO}}, \omega_{\mathrm{LO}} \pm \omega_{\mathrm{IF}}$. Only the lower one at $\omega_{\mathrm{LO}} - \omega_{\mathrm{IF}}$ is retained to avoid affecting other qubits. The other two components at ω_{LO} and $\omega_{\mathrm{LO}} + \omega_{\mathrm{IF}}$ are blocked by adjusting the IQ phase difference $|\phi_I - \phi_Q|$ and controlling the IQ ratio V_I/V_Q. Therefore, the drive frequency ω_d is tuned by control LO frequency and IF frequency at the output port:

$$\omega_d = \omega_{\mathrm{LO}} - \omega_{\mathrm{IF}}. \tag{3.4}$$

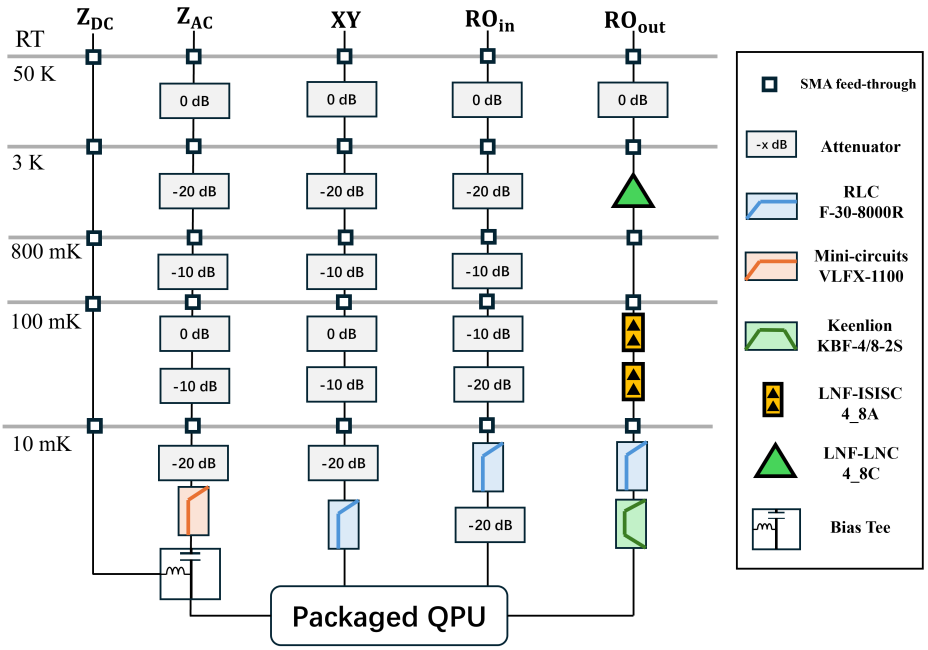

Figure 3.4: Wiring diagram of the experimental setup in the qubit control and measurement.

The wiring diagram in Fig. 3.4 demonstrates how signals are sent to the quantum chip operating below 10 mK in the dilution refrigerator. The attenuators are used to eliminate the thermal noise by reducing signal power. After a series of attenuators and low-pass filters in the fridge, the drive signal reaches the QPU via a capacitor. The coupler frequency is tuned by changing the flux, which is generated by the combination of biased DC current from S4g (QBLOX instrument) and AC current from QCM (QBLOX Instruments). The AC and DC signal is coupled via a bias tee before arriving at QPU. In the qubit readout, the signal coming from QPU is amplified by low-noise amplifiers (LNF-ISISC4_8A and LNF-LNC4_8C). In a dilution refrigerator, feed-throughs connect different devices in different cooling stages.

3.3 Calibration of QC SWAP gate

Here, in Fig. 3.5, we show the pulse scheme for calibrating QC SWAP.

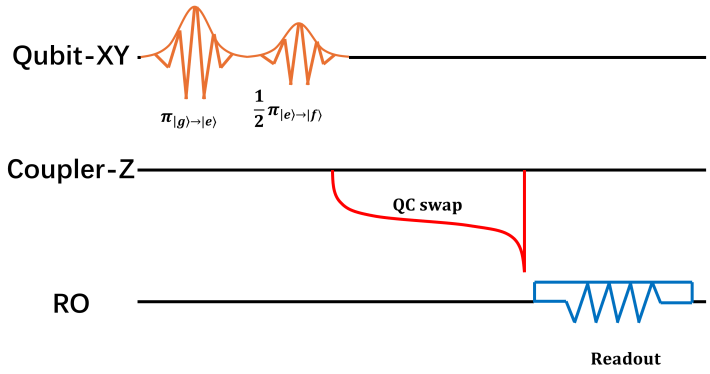

Figure 3.5: Pulse scheme of calibrating QC SWAP gate in qubit reset.

Since our goal is to reset the qubit from any superposition of $|e\rangle$ and $|f\rangle$ to ground state $|g\rangle$, the qubit is first driven by a π pulse at transition frequency $f_{|g\rangle\to|e\rangle}$ and followed by a $\pi/2$ pulse at transition frequency $f_{|e\rangle\to|f\rangle}$, thus initializing the qubit into $(|e\rangle + |f\rangle)/\sqrt{2}$. After qubit initialization, the QC SWAP gate is implemented to transfer excitation from qubit to coupler. A readout pulse is then applied to the readout resonator through the feedline, and the population in qubit is measured.

There are four parameters to be calibrated: initial coupler frequency $f_c(0)$, final coupler frequency $f_c(T)$, coupling strength (pulse shape) $\bar{g}$ and duration T, indicating that the calibration requires intensive computation resources in four-dimensional parameter search space. This complexity can be reduced by fixing one or two of the parameters and calibrating the remaining ones. In the simulation, we first sweep the final frequency $f_c(T)$ and duration T by fixing the initial frequency $f_c(0)$ and pulse shape $\bar{g}$. The second calibration sweeps the pulse shape $\bar{g}$ and duration T with the optimal final frequency $f_{c_{\text{opt}}}(T)$ found in the first stage of the first calibration.

In the experiment, we sweep parameters in the $f_c(T)$-T space in the first stage, and $f_c(0)$-$\bar{g}$ in a second stage.

4

Results

In this chapter, we present results from both simulations and experiments. We examine the RC protocol-based flux pulse by tracking the reset error and adiabaticity throughout the evolution. All device parameters used in the simulation and experiment are listed in Tab. 4.1.

Parameters		Q_0	Q_1
Qubit frequency	$\omega_q/2\pi$ (GHz)	5.176	4.534
Qubit anharmonicity	$\alpha/2\pi$ (MHz)	-256	-158
Qubit-coupler coupling	$g/2\pi$ (MHz)	47	64

Table 4.1: Device parameters from measurement [1].

4.1 Simulation results

Simulations are carried out using QuTiP, a toolbox for simulating quantum systems [69, 70]. A qubit-coupler-qubit system (denoted by $Q_0C_0Q_1$) can be described by a Hamiltonian:

$$H = \sum_{i=0,1} \omega_i a_i^\dagger a_i + \frac{\alpha_i}{2} a_i^\dagger a_i^\dagger a_i a_i + \omega_c(t) b^\dagger b + g_{0c}(a_0^\dagger b + a_0 b^\dagger) + g_{1c}(a_1^\dagger b + a_1 b^\dagger), \quad (4.1)$$

where ω_0 and ω_1 denote the bare qubit frequencies of Q_0 and Q_1 with their qubit anharmonicities α_0 and α_1. The tunable coupler with tunable frequency $\omega_c(t)$ is coupled to Q_0 and Q_1 with coupling rate g_{0c} and g_{1c}.

In the QC SWAP stage, we aim to adiabatically move all the excitation in Q_0 to C_0. Specifically, the target states we want to populate are $|Q_0C_0Q_1\rangle = |010\rangle$ and $|Q_0C_0Q_1\rangle = |020\rangle$ such that all excitation is transferred to the coupler, and transition to all other states contributes to the reset error, denoted by ϵ:

$$\epsilon = 1 - (|\langle\psi(T)|010\rangle|^2 + |\langle\psi(T)|020\rangle|^2), \quad (4.2)$$

where T is the duration of QC SWAP gate and $|\psi(T)\rangle$ is the final state after gate operation. The error in the QC SWAP gate arises from two main sources: population left in the Q_0 due to diabatic oscillations and leakage to Q_1 that we don't want to populate. For example, in $|e\rangle$-state reset, the error is the sum of the population in states $|100\rangle$ and $|001\rangle$:

$$\epsilon_{|e\rangle} = |\langle\psi(T)|100\rangle|^2 + |\langle\psi(T)|001\rangle|^2, \tag{4.3}$$

where the first term and the second term represent the diabatic error and the leakage to Q_1.

In the first step of our calibration, given the analytical expression of QC SWAP pulse in Eq. (2.107), we set the shape parameter $\bar{g}$ to be 47 MHz and the initial point of coupler frequency $f_c(0) = \omega_c(0)/2\pi$ to be 6.032 GHz. Next, we sweep through two parameters: duration T of the flux pulse and final coupler frequency $f_c(T) = \omega_c(T)/2\pi$. We then fix $f_c(T)$ where reset error ϵ is minimal in $f_c(T) - T$ search space. The swap operation is further optimized by fine-tuning the pulse parameter $\bar{g}$ and duration T in a 2D landscape.

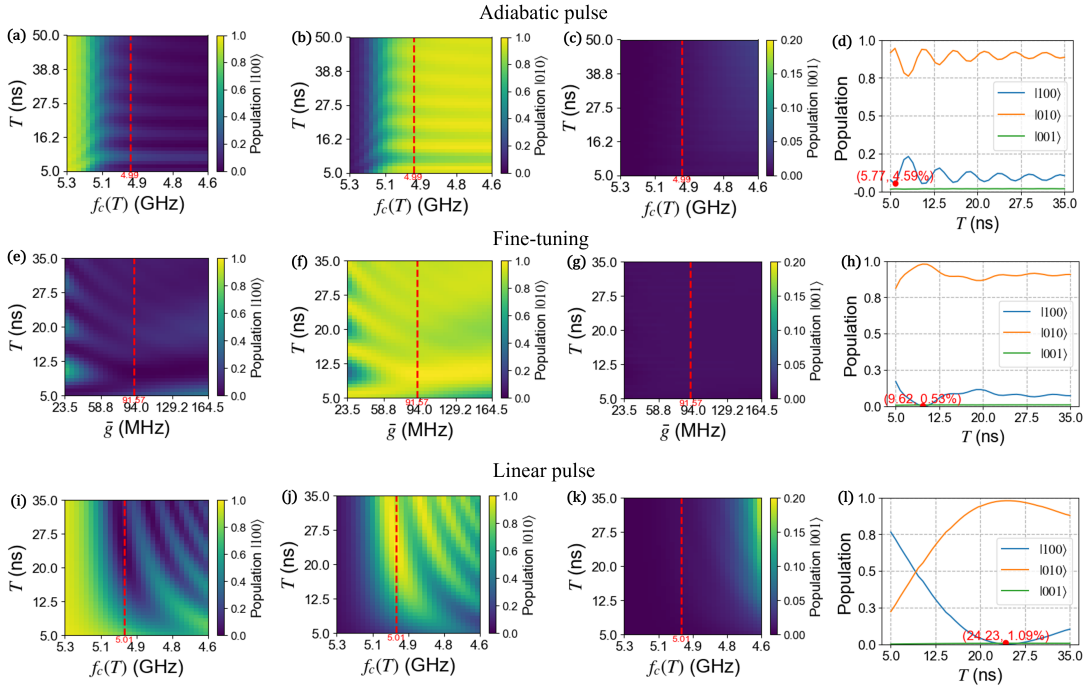

Figure 4.1: Calibration results of adiabatic pulse and linear pulse in QC SWAP gate for resetting the qubit $|e\rangle$-state. Parameters in the calibration: final coupler frequency $f_c(T)$, pulse duration T and shape parameter $\bar{g}$. Each point in the 2D sweeps represents the population of states $|100\rangle$, $|010\rangle$ and $|001\rangle$ in calibrating **(a-c)** adiabatic pulse, **(e-g)** fine-tuning of the adiabatic pulse and **(i-k)** linear pulse. The line-cuts in **(d, h, l)** are taken from the 2D parameter search space, represented by a vertical red dashed line. The red dots in the line-cuts mark the optimal parameters and the corresponding reset error ϵ.

We first calibrate the QC SWAP gate for only $|e\rangle$-state reset. In the calibration, the target qubit to be reset is excited to $|e\rangle$ by a π gate, followed by the adiabatic

pulse with different pulse parameters and a readout pulse afterward. The results of all calibrations for the adiabatic pulse, including a linear pulse for comparison, are shown in Fig. 4.1.

In Fig. 4.1(a-d), we search for the optimal point for $f_c(T)$ from 4.6 GHz to 5.3 GHz where the error ϵ is minimal. We then fix $f_c(T)$ to be 4.99 GHz and find the lowest reset error to be 0.53% within only 9.02 ns with $\bar{g} = 92$ MHz, (Fig. 4.1(e-h)), while it takes 24.23 ns for a linear pulse with the same $f_c(0)$ and $f_c(T)$ to reach an error rate of 1.09% (Fig. 4.1(i-l)).

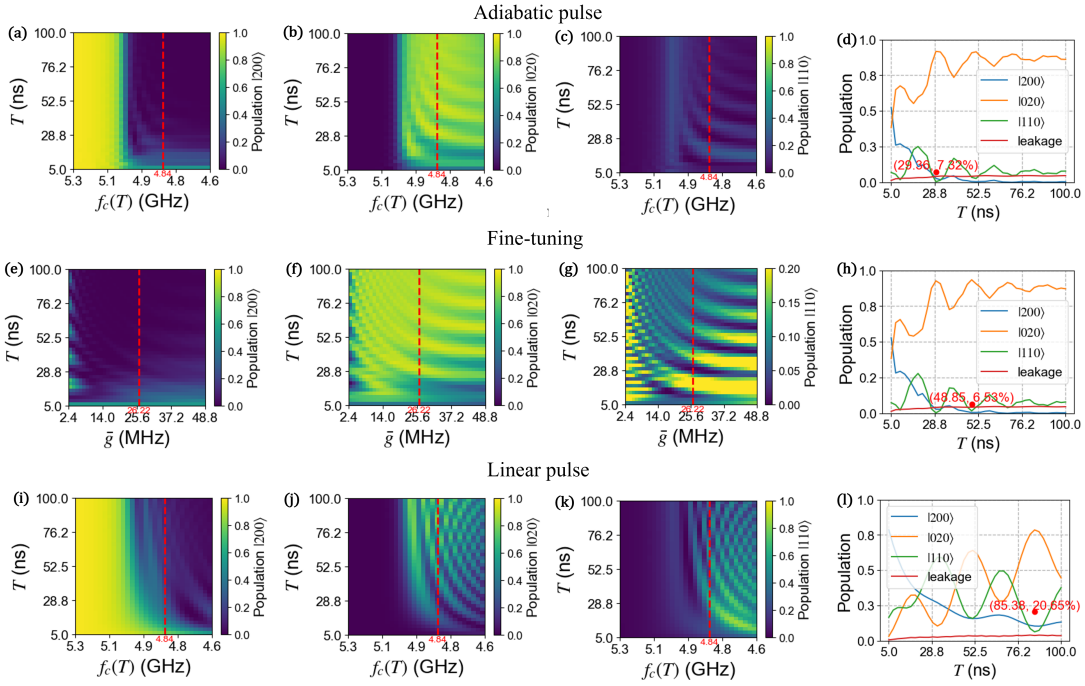

Figure 4.2: Calibration results of adiabatic pulse and linear pulse in QC SWAP gate for resetting the qubit $|f\rangle$-state. Parameters in the calibration: final coupler frequency $f_c(T)$, pulse duration T, and shape parameter $\bar{g}$. Each point in the 2D sweeps represents the population of states $|200\rangle$, $|020\rangle$ and $|110\rangle$ in calibrating **(a-c)** adiabatic pulse, **(e-g)** fine-tuning of the adiabatic pulse and **(i-k)** linear pulse. The line-cuts in **(d, h, l)** are taken from the 2D parameter search space, represented by a vertical red dashed line. The red dots in the line-cuts mark the optimal parameters and the corresponding reset error $\epsilon_{|e\rangle}$.

For resetting the $|f\rangle$-state (Fig. 4.2), the calibration protocol follows the same structure, with the initial state being $|200\rangle$. In this case, the reset error is defined as:

$$\epsilon_{|f\rangle} = 1 - |\langle\psi|020\rangle|^2. \tag{4.4}$$

Fig. 4.2 illustrates calibrations results for $|f\rangle$-state reset. In Fig. 4.2(a, d), the adiabatic pulse depopulates state $|200\rangle$ within only 53 ns, while the linear pulse cannot

depopulate all the population in $|200\rangle$ within 100 ns, with 15% of the population left in $|f\rangle$-level (Fig. 4.2(l)). Fig. 4.2(d) also shows that with increasing pulse duration T, $|020\rangle$ is adiabatically populated and the diabatic swap between the target state $|020\rangle$ and the intermediate state $|110\rangle$ is mitigated, achieving an error rate of 6.53% after fine-tuning (Fig. 4.2(h)). Fig. 4.2(j, k) shows that the linear pulse doesn't follow an adiabatic path as state $|20\rangle$ is not adiabatically populated with longer duration, and the diabatic swap between $|020\rangle$ and $|110\rangle$ limits the performance of the reset gate, with a minimal error rate of 20.65% at best (Fig. 4.2(l)).

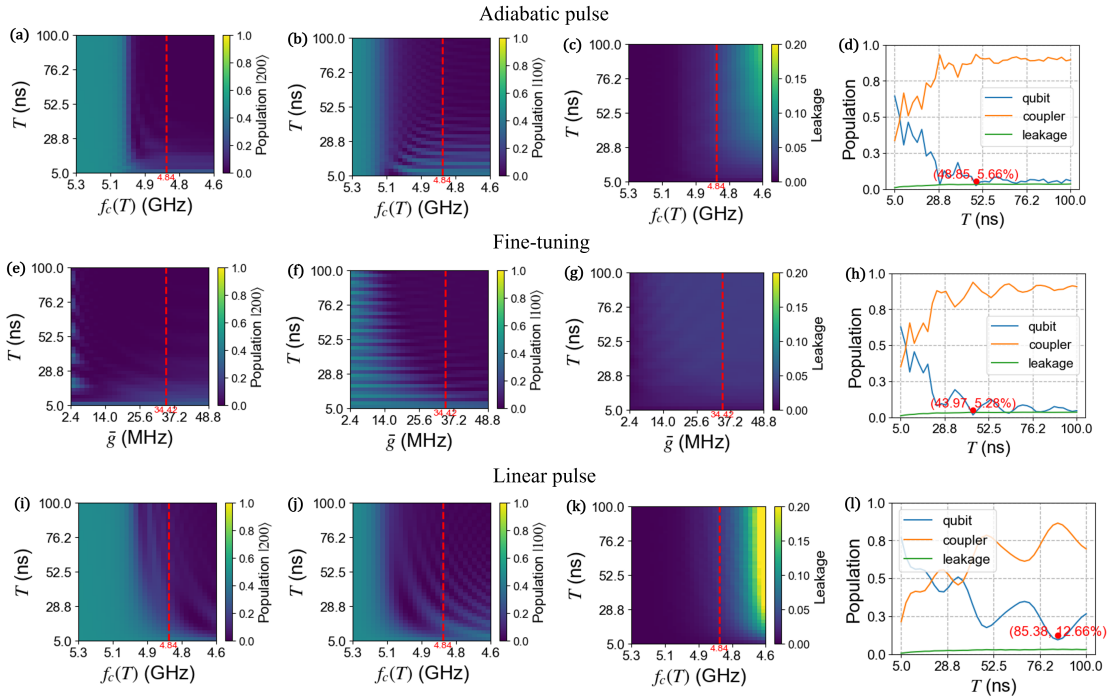

Figure 4.3: Calibration results of adiabatic pulse and linear pulse in QC swap gate for resetting qubit with the state prepared in $(|200\rangle + |100\rangle)/\sqrt{2}$**.** Each point in the 2D sweeps represents the population of state $|200\rangle$, $|100\rangle$ and leakage p_l in calibrating **(a-c)** adiabatic pulse, **(e-g)** fine-tuning of the adiabatic pulse and **(i-k)** linear pulse. The line-cuts in **(d, h, l)** are taken from the 2D parameter search space, represented by the vertical red dashed lines. The red dots in the line-cuts mark the optimal parameters and the corresponding reset errors $\epsilon_{|f\rangle}$.

To calibrate the QC SWAP gate for resetting $|e\rangle$-state and $|f\rangle$-state at once, the state is initialized to be $(|1\rangle + |2\rangle)/\sqrt{2}$ and the results are shown in Fig. 4.3. The population in the qubit Q_0, coupler C_0 and the leakage to Q_1, denoted by p_q, p_c, p_l are defined as:

$$p_q = |\langle\psi(T)|200\rangle|^2 + |\langle\psi(T)|110\rangle|^2 + |\langle\psi(T)|100\rangle|^2 \tag{4.5}$$

$$p_c = |\langle\psi(T)|020\rangle|^2 + |\langle\psi(T)|010\rangle|^2 \tag{4.6}$$

$$p_l = 1 - (p_q + p_c) \tag{4.7}$$

Fig. 4.3(d, h) illustrates that the reset error rate can reach below 6% within 100 ns, giving advantages in reset fidelity and speed when compared to the error achieved with a linear pulse shape, as shown in Fig. 4.3(l). However, the leakage to Q_1 becomes not negligible as the coupler frequency (4.86 GHz) is moved very close to the qubit frequency (4.534 GHz) since the population in Q_1 is estimated to be around 5% (Fig. 4.2(d, h, l) and Fig. 4.3(d, h, l)). Therefore, we need to consider a tradeoff between low leakage and high QC swap fidelity. Another interesting finding is that when the coupler frequency is brought to around 4.6 GHz, which is very close to the avoided-crossing with Q_1, utilizing adiabatic pulse gives less perturbation compared to the linear pulse shape, as shown in Fig. 4.1(c, k) and Fig. 4.3(c, k).

All the results suggest that, with careful calibration, we can accelerate the QC SWAP operation following adiabatic or STA paths, given the RC protocol. However, the presence of another qubit coupled to the tunable coupler greatly hinders the reset protocol from achieving high fidelity due to unavoidable leakage, especially in the case of resetting $|f\rangle$-state. This is because when the coupler frequency is moved near the avoided-crossing regime where $|200\rangle$ interacts with $|002\rangle$ via intermediate state $|110\rangle$, it also interacts with the other qubit, causing the excitation swap between C_0 and Q_1. Another advantage of the adiabatic pulse is it is resilient to slight drift in pulse parameters (see the 2D landscape in Fig. 4.1(a,b,e,f)). However, since it is not possible to achieve perfect adiabatic evolution, there is always diabatic oscillation in the results (Fig. 4.1(d,h,l)).

4.2 Experiment results

Here, we show only the results of calibrating the QC SWAP gate to reset the qubit state prepared in $|e\rangle$ and $(|e\rangle + |f\rangle)/\sqrt{2}$, as illustrated in Fig. 4.4 taken from our recent manuscript [1]. In the experiment, there are four parameters to be optimized: $f_c(0)$ and $f_c(T)$ specify the initial and final coupler frequency, with T being the pulse duration and $\bar{g}$ controlling the shape of the pulse.

Both in simulation and experiment, the QC SWAP gate can reset qubit from $|e\rangle$-state to $|g\rangle$-state in around 9 ns (Fig. 4.1(h) and Fig. 4.4(b, d)) with error rate reaching below 1%.

We apply the same calibration protocol in $|e\rangle$-state and $|f\rangle$-state reset, finding the optimal $barg$ to be 200 MHz and T to be 31 ns with reset error of around 5% (see Fig. 4.4(f, h)), close to the estimated error in our simulation (Fig. 4.3(h)).

To further remove the residual population in Q_0, instead of only one coupler, we can use two tunable couplers coupled to the target qubit to apply two QC SWAP gates for each coupler sequentially. More specifically, the target qubit Q_0 swaps excitation into two couplers: C_0 and C_1 as shown in Fig. 4.5. We can first apply a QC SWAP pulse between Q_0 and C_0, then a second one between Q_0 and C_1. In the end, these two couplers are then biased to interact with R_0.

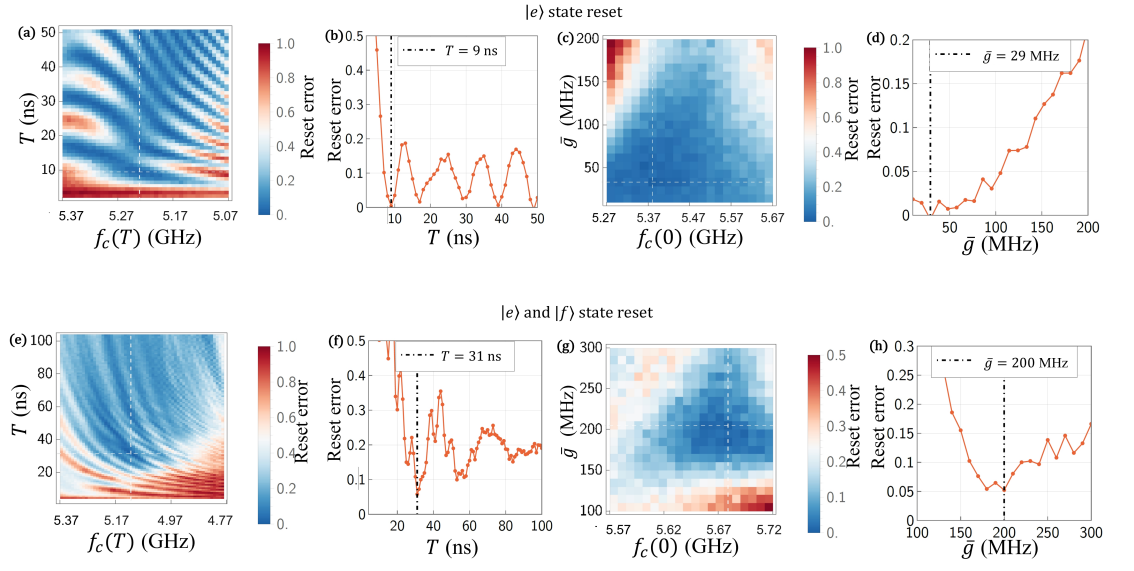

Figure 4.4: Calibration results of the QC SWAP gate with qubit prepared in the state $|e\rangle$ (a-d) and $(|e\rangle + |f\rangle)/\sqrt{2}$ (e-h) from Ref. [1]. (a, c, e, g) Each point in the 2D sweep represents the population left in the qubit (except $|g\rangle$) as the reset error. Each line-cut shown in **(b, d, f, h)** is the cross-section from the 2D sweep **(a, c, e, g)** respectively, and indicated by the dashed lines.

With this improved protocol, experiments show that in resetting $|e\rangle$ and $|f\rangle$ simultaneously, the reset error rate is 0.787% using only 61 ns for two QC SWAP operations [1].

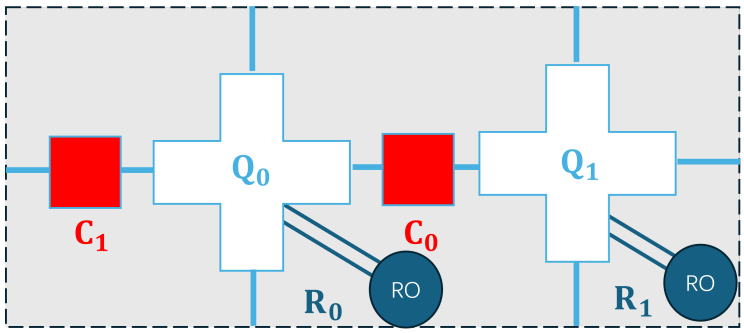

Figure 4.5: Subset of qubits, couplers, and readout resonators used in two sequential QC SWAP gates.

5

Conclusion & Discussion

In this thesis, we have theoretically devised a QC SWAP gate for qubit reset and shown the results both in simulations and experiments. We first review the circuit quantum electrodynamics and introduce the quantization of transmon qubits to obtain a Hamiltonian of a system consisting of two fixed-frequency qubits and a tunable coupler. Next, we have shown that the adiabatic evolution of qubit $|e\rangle$-state reset is identified as a Z-field control in a two-level system. Based on this model, one can derive a parametric, analytical expression of adiabatic pulse using Roland-Cerf protocol. In the simulation, we find that the adiabaticity of the evolution is tunable by varying the shape parameter $\bar{g}$. For some parameters, the evolution follows a shortcut-to-adiabaticity path, accelerating the qubit reset. To achieve $|f\rangle$-state reset, following the RC protocol, we need to reduce the three-level system to a two-level system in a weak perturbative regime. The validity of isolating the low eigenstates in adiabatic evolution is supported by Kato's adiabatic theorem [54] and formulation in Ref. [51]. We use non-perturbative adiabatic diagonalization and Schrieffer–Wolff transformation to perform block-diagonalization, allowing us to obtain an effective TLS Hamiltonian in the subspace of the two lowest eigenstates. Based on the effective Hamiltonians, we derive the analytical expression of the adiabatic pulse for resetting the $|f\rangle$-state. In calibrating the parametric pulse with four parameters, we reduce the four-dimensional parameter search space into two separate calibration stages in a two-dimensional parameter space.

The simulations demonstrate that the QC SWAP gate can reset $|e\rangle(|f\rangle)$-state in around 9 ns (48.85 ns) with an error rate of 0.53% (6.53%). For unconditionally resetting both $|e\rangle$-state and $|f\rangle$-state at once, it takes 43.97 ns to achieve an error rate of 5.28%. In our experiment, the QC SWAP gate gives an error rate of around 5%, which can be minimized by performing another QC SWAP gate with an additional coupler, and the full reset protocol results in a reset error below 1% for both $|e\rangle$-state and $|f\rangle$-state within 83 ns [1].

Many sources are contributing to the error in the QC SWAP gate. One of the major errors comes from the leakage to other irrelevant eigenstates and also the leakage to the other coupled qubit in $|f\rangle$-state reset where the coupler is moved very close to the non-target qubit. Also, as the evolution is not perfectly adiabatic, we can always find the diabatic oscillation over time, which can be mitigated by calibrating pulse parameters. The effectiveness of the TLS model can also contribute to the error mentioned above. In the experiment, the imprecise pulse shape due to flux pulse distortion and the sampling period of AWG could also limit the overall performance

of the reset protocol.

To further improve the reset fidelity, it is desirable to find the relation between the leakage errors and hardware parameters (qubit detuning, coupling rate, etc.) so that the reset error can be considered while designing a new device. Another possible improvement is finding a new adiabatic or STA path based on different forms of the RC protocol or other protocols that are not based on the spectrum analysis. Another key point is that there should be a better block-diagonalization technique existing under the approximate adiabatic condition since there are many ways to arrive at different effective TLS Hamiltonians. Furthermore, as the adiabatic condition in the RC protocol is sufficient for most models, we also expect that it is possible to implement the same protocol and calibration in other quantum controls where accelerating the adiabatic process is needed.

Bibliography

[1] Liangyu Chen, Simon Pettersson Fors, Zixian Yan, Anaida Ali, Tahereh Abad, Amr Osman, Eleftherios Moschandreou, Benjamin Lienhard, Sandoko Kosen, Hang-Xi Li, et al. Fast unconditional reset and leakage reduction in fixed-frequency transmon qubits. *arXiv preprint arXiv:2409.16748*, 2024.

[2] Richard P Feynman. Simulating physics with computers. In *Feynman and computation*, pages 133–153. cRc Press, 2018.

[3] David Deutsch. Quantum theory, the church–turing principle and the universal quantum computer. *Proceedings of the Royal Society of London. A. Mathematical and Physical Sciences*, 400(1818):97–117, 1985.

[4] David Deutsch and Richard Jozsa. Rapid solution of problems by quantum computation. *Proceedings of the Royal Society of London. Series A: Mathematical and Physical Sciences*, 439(1907):553–558, 1992.

[5] Daniel R Simon. On the power of quantum computation. *SIAM journal on computing*, 26(5):1474–1483, 1997.

[6] Peter W Shor. Algorithms for quantum computation: discrete logarithms and factoring. In *Proceedings 35th annual symposium on foundations of computer science*, pages 124–134. Ieee, 1994.

[7] Michael A Nielsen and Isaac L Chuang. *Quantum computation and quantum information*, volume 2. Cambridge university press Cambridge, 2001.

[8] Edward Farhi, Jeffrey Goldstone, and Sam Gutmann. A quantum approximate optimization algorithm. *arXiv preprint arXiv:1411.4028*, 2014.

[9] Alberto Peruzzo, Jarrod McClean, Peter Shadbolt, Man-Hong Yung, Xiao-Qi Zhou, Peter J Love, Alán Aspuru-Guzik, and Jeremy L O'brien. A variational eigenvalue solver on a photonic quantum processor. *Nature communications*, 5(1):4213, 2014.

[10] Nikolaj Moll, Panagiotis Barkoutsos, Lev S Bishop, Jerry M Chow, Andrew Cross, Daniel J Egger, Stefan Filipp, Andreas Fuhrer, Jay M Gambetta, Marc Ganzhorn, et al. Quantum optimization using variational algorithms on near-term quantum devices. *Quantum Science and Technology*, 3(3):030503, 2018.

[11] Philipp Hauke, Helmut G Katzgraber, Wolfgang Lechner, Hidetoshi Nishimori, and William D Oliver. Perspectives of quantum annealing: Methods and implementations. *Reports on Progress in Physics*, 83(5):054401, 2020.

[12] Earl T Campbell, Hussain Anwar, and Dan E Browne. Magic-state distillation in all prime dimensions using quantum reed-muller codes. *Physical Review X*, 2(4):041021, 2012.

[13] Nikita Kolganov, Sergey Mironov, and Andrey Morozov. Large k topological quantum computer. *Nuclear Physics B*, 987:116072, 2023.

[14] S. P. Walborn, D. S. Lemelle, M. P. Almeida, and P. H. Souto Ribeiro. Quantum key distribution with higher-order alphabets using spatially encoded qudits. *Phys. Rev. Lett.*, 96:090501, Mar 2006.

[15] Youngseok Kim, Andrew Eddins, Sajant Anand, Ken Xuan Wei, Ewout Van Den Berg, Sami Rosenblatt, Hasan Nayfeh, Yantao Wu, Michael Zaletel, Kristan Temme, et al. Evidence for the utility of quantum computing before fault tolerance. *Nature*, 618(7965):500–505, 2023.

[16] Abe Asfaw, Anthony Megrant, Cody Jones, Craig Gidney, Dave Bacon, Dripto Debroy, Dvir Kafri, Erik Lucero, Hartmut Neven, Jeremy Hilton, Jimmy Chen, John Platt, Jonathan Gross, Juan Atalaya, Julian Kelly, Kenny Lee, Kevin Satzinger, Michael Newman, Sergio Boixo, Vadim Smelyanskiy, Yu Chen, and Catherine Vollgraff Heidweiller. Suppressing quantum errors by scaling a surface code logical qubit. *Nature*, 614(7949):676–681, 2023.

[17] Sebastian Krinner, Nathan Lacroix, Ants Remm, Agustin Di Paolo, Elie Genois, Catherine Leroux, Christoph Hellings, Stefania Lazar, Francois Swiadek, Johannes Herrmann, et al. Realizing repeated quantum error correction in a distance-three surface code. *Nature*, 605(7911):669–674, 2022.

[18] Sandoko Kosen, Hang-Xi Li, Marcus Rommel, Daryoush Shiri, Christopher Warren, Leif Grönberg, Jaakko Salonen, Tahereh Abad, Janka Biznárová, Marco Caputo, et al. Building blocks of a flip-chip integrated superconducting quantum processor. *Quantum Science and Technology*, 7(3):035018, 2022.

[19] Fernando Valadares, Ni-Ni Huang, Kyle Timothy Ng Chu, Aleksandr Dorogov, Weipin Chua, Lingda Kong, Pengtao Song, and Yvonne Y Gao. On-demand transposition across light-matter interaction regimes in bosonic cqed. *Nature Communications*, 15(1):5816, 2024.

[20] Youwei Zhao, Yangsen Ye, He-Liang Huang, Yiming Zhang, Dachao Wu, Huijie Guan, Qingling Zhu, Zuolin Wei, Tan He, Sirui Cao, Fusheng Chen, Tung-Hsun Chung, Hui Deng, Daojin Fan, Ming Gong, Cheng Guo, Shaojun Guo, Lianchen Han, Na Li, Shaowei Li, Yuan Li, Futian Liang, Jin Lin, Haoran Qian, Hao Rong, Hong Su, Lihua Sun, Shiyu Wang, Yulin Wu, Yu Xu, Chong Ying, Jiale Yu, Chen Zha, Kaili Zhang, Yong-Heng Huo, Chao-Yang Lu, Cheng-Zhi Peng, Xiaobo Zhu, and Jian-Wei Pan. Realization of an error-correcting surface code with superconducting qubits. *Phys. Rev. Lett.*, 129:030501, Jul 2022.

[21] John M Martinis, Michel H Devoret, and John Clarke. Energy-level quantization in the zero-voltage state of a current-biased josephson junction. *Physical review letters*, 55(15):1543, 1985.

[22] Yasunobu Nakamura, Chii Dong Chen, and Jaw Shen Tsai. Spectroscopy of energy-level splitting between two macroscopic quantum states of charge coherently superposed by josephson coupling. *Physical review letters*, 79(12):2328, 1997.

[23] Yasunobu Nakamura, Yu A Pashkin, and JS Tsai. Coherent control of macroscopic quantum states in a single-cooper-pair box. *nature*, 398(6730):786–788, 1999.

[24] Terry P. Orlando, Lin Tian, Leonid Levitov, Seth Lloyd, Donald S. Crankshaw, Juan J. Mazo, Johann E. Mooij, C. H. Wal, A. C. Wallast, and C. Harmans.

Superconducting persistent-current qubit. *Physical Review B*, 60:15398–15413, 1999.

[25] JE Mooij, TP Orlando, L Levitov, Lin Tian, Caspar H Van der Wal, and Seth Lloyd. Josephson persistent-current qubit. *Science*, 285(5430):1036–1039, 1999.

[26] John M. Martinis, S. Nam, J. Aumentado, and C. Urbina. Rabi oscillations in a large josephson-junction qubit. *Phys. Rev. Lett.*, 89:117901, Aug 2002.

[27] AJ Berkley, H Xu, RC Ramos, MA Gubrud, FW Strauch, PR Johnson, JR Anderson, AJ Dragt, CJ Lobb, and FC Wellstood. Entangled macroscopic quantum states in two superconducting qubits. *Science*, 300(5625):1548–1550, 2003.

[28] Jens Koch, Terri M. Yu, Jay Gambetta, A. A. Houck, D. I. Schuster, J. Majer, Alexandre Blais, M. H. Devoret, S. M. Girvin, and R. J. Schoelkopf. Charge-insensitive qubit design derived from the cooper pair box. *Phys. Rev. A*, 76:042319, Oct 2007.

[29] Rami Barends, Julian Kelly, Anthony Megrant, Andrzej Veitia, Daniel Sank, Evan Jeffrey, Ted C White, Josh Mutus, Austin G Fowler, Brooks Campbell, et al. Superconducting quantum circuits at the surface code threshold for fault tolerance. *Nature*, 508(7497):500–503, 2014.

[30] Julian Kelly, Rami Barends, Austin G Fowler, Anthony Megrant, Evan Jeffrey, Theodore C White, Daniel Sank, Josh Y Mutus, Brooks Campbell, Yu Chen, et al. State preservation by repetitive error detection in a superconducting quantum circuit. *Nature*, 519(7541):66–69, 2015.

[31] Antonio D Córcoles, Easwar Magesan, Srikanth J Srinivasan, Andrew W Cross, Matthias Steffen, Jay M Gambetta, and Jerry M Chow. Demonstration of a quantum error detection code using a square lattice of four superconducting qubits. *Nature communications*, 6(1):6979, 2015.

[32] Frank Arute, Kunal Arya, Ryan Babbush, Dave Bacon, Joseph C Bardin, Rami Barends, Rupak Biswas, Sergio Boixo, Fernando GSL Brandao, David A Buell, et al. Quantum supremacy using a programmable superconducting processor. *Nature*, 574(7779):505–510, 2019.

[33] D Ristè, CC Bultink, Konrad W Lehnert, and L DiCarlo. Feedback control of a solid-state qubit using high-fidelity projective measurement. *Physical review letters*, 109(24):240502, 2012.

[34] P. Campagne-Ibarcq, E. Flurin, N. Roch, D. Darson, P. Morfin, M. Mirrahimi, M. H. Devoret, F. Mallet, and B. Huard. Persistent control of a superconducting qubit by stroboscopic measurement feedback. *Phys. Rev. X*, 3:021008, May 2013.

[35] MS Moreira, Gian Giacomo Guerreschi, Wouter Vlothuizen, Jorge F Marques, Jeroen van Straten, Shavindra P Premaratne, Xiang Zou, Hany Ali, Nandini Muthusubramanian, Christos Zachariadis, et al. Realization of a quantum neural network using repeat-until-success circuits in a superconducting quantum processor. *npj Quantum Information*, 9(1):118, 2023.

[36] Sergio O Valenzuela, William D Oliver, David M Berns, Karl K Berggren, Leonid S Levitov, and Terry P Orlando. Microwave-induced cooling of a superconducting qubit. *Science*, 314(5805):1589–1592, 2006.

[37] Matthew D Reed, Blake R Johnson, Andrew A Houck, Leonardo DiCarlo, Jerry M Chow, David I Schuster, Luigi Frunzio, and Robert J Schoelkopf.

Fast reset and suppressing spontaneous emission of a superconducting qubit. *Applied Physics Letters*, 96(20), 2010.

[38] Kurtis Geerlings, Zaki Leghtas, Ioan M Pop, Shyam Shankar, Luigi Frunzio, Robert J Schoelkopf, Mazyar Mirrahimi, and Michel H Devoret. Demonstrating a driven reset protocol for a superconducting qubit. *Physical review letters*, 110(12):120501, 2013.

[39] Daniel J Egger, Max Werninghaus, Marc Ganzhorn, Gian Salis, Andreas Fuhrer, Peter Müller, and Stefan Filipp. Pulsed reset protocol for fixed-frequency superconducting qubits. *Physical Review Applied*, 10(4):044030, 2018.

[40] Matt McEwen, Dvir Kafri, Z Chen, Juan Atalaya, KJ Satzinger, Chris Quintana, Paul Victor Klimov, Daniel Sank, C Gidney, AG Fowler, et al. Removing leakage-induced correlated errors in superconducting quantum error correction. *Nature communications*, 12(1):1761, 2021.

[41] Xiaohan Yang, Ji Chu, Zechen Guo, Wenhui Huang, Yongqi Liang, Jiawei Liu, Jiawei Qiu, Xuandong Sun, Ziyu Tao, Jiawei Zhang, et al. Coupler-assisted leakage reduction for scalable quantum error correction with superconducting qubits. *arXiv preprint arXiv:2403.16155*, 2024.

[42] Alexandre Blais, Ren-Shou Huang, Andreas Wallraff, Steven M Girvin, and R Jun Schoelkopf. Cavity quantum electrodynamics for superconducting electrical circuits: An architecture for quantum computation. *Physical Review A—Atomic, Molecular, and Optical Physics*, 69(6):062320, 2004.

[43] Andreas Wallraff, David I Schuster, Alexandre Blais, Luigi Frunzio, R-S Huang, Johannes Majer, Sameer Kumar, Steven M Girvin, and Robert J Schoelkopf. Strong coupling of a single photon to a superconducting qubit using circuit quantum electrodynamics. *Nature*, 431(7005):162–167, 2004.

[44] Nathan K Langford. Circuit qed-lecture notes. *arXiv preprint arXiv:1310.1897*, 2013.

[45] Uri Vool and Michel Devoret. Introduction to quantum electromagnetic circuits. *International Journal of Circuit Theory and Applications*, 45(7):897–934, 2017.

[46] Steven M Girvin. Circuit qed: superconducting qubits coupled to microwave photons, 2014.

[47] Philip Krantz, Morten Kjaergaard, Fei Yan, Terry P Orlando, Simon Gustavsson, and William D Oliver. A quantum engineer's guide to superconducting qubits. *Applied physics reviews*, 6(2), 2019.

[48] Brian David Josephson. Possible new effects in superconductive tunnelling. *Physics letters*, 1(7):251–253, 1962.

[49] BRIAN D Josephson. The discovery of tunnelling supercurrents. *Reviews of Modern Physics*, 46(2):251, 1974.

[50] John R Waldram. *Superconductivity of metals and cuprates*. CRC Press, 2017.

[51] Evgeny Mozgunov and Daniel A Lidar. Quantum adiabatic theorem for unbounded hamiltonians with a cutoff and its application to superconducting circuits. *Philosophical Transactions of the Royal Society A*, 381(2241):20210407, 2023.

[52] Jun John Sakurai and Jim Napolitano. *Modern quantum mechanics*. Cambridge University Press, 2020.

[53] Daniel Comparat. General conditions for quantum adiabatic evolution. *Physical Review A—Atomic, Molecular, and Optical Physics*, 80(1):012106, 2009.

[54] Tosio Kato. On the adiabatic theorem of quantum mechanics. *Journal of the Physical Society of Japan*, 5(6):435–439, 1950.

[55] J. E. Avron and A. Elgart. Adiabatic theorem without a gap condition: Two-level system coupled to quantized radiation field. *Phys. Rev. A*, 58:4300–4306, Dec 1998.

[56] Joseph E Avron and Alexander Elgart. Adiabatic theorem without a gap condition. *Communications in mathematical physics*, 203:445–463, 1999.

[57] Jérémie Roland and Nicolas J Cerf. Quantum search by local adiabatic evolution. *Physical Review A*, 65(4):042308, 2002.

[58] Mark G Bason, Matthieu Viteau, Nicola Malossi, Paul Huillery, Ennio Arimondo, Donatella Ciampini, Rosario Fazio, Vittorio Giovannetti, Riccardo Mannella, and Oliver Morsch. High-fidelity quantum driving. *Nature Physics*, 8(2):147–152, 2012.

[59] N. Malossi, M. G. Bason, M. Viteau, E. Arimondo, R. Mannella, O. Morsch, and D. Ciampini. Quantum driving protocols for a two-level system: From generalized Landau-Zener sweeps to transitionless control. *Physical Review A*, 87:012116, Jan 2013.

[60] Dionisis Stefanatos and Emmanuel Paspalakis. Resonant shortcuts for adiabatic rapid passage with only z-field control. *Physical Review A*, 100:012111, Jul 2019.

[61] F. Petiziol, B. Dive, S. Carretta, R. Mannella, F. Mintert, and S. Wimberger. Accelerating adiabatic protocols for entangling two qubits in circuit qed. *Physical Review A*, 99:042315, Apr 2019.

[62] Boxi Li, Tommaso Calarco, and Felix Motzoi. Nonperturbative analytical diagonalization of hamiltonians with application to circuit qed. *PRX Quantum*, 3(3):030313, 2022.

[63] Joaquin M Luttinger and Walter Kohn. Motion of electrons and holes in perturbed periodic fields. *Physical Review*, 97(4):869, 1955.

[64] John R Schrieffer and Peter A Wolff. Relation between the anderson and kondo hamiltonians. *Physical Review*, 149(2):491, 1966.

[65] R Winkler, S Papadakis, E De Poortere, and M Shayegan. *Spin-orbit coupling in two-dimensional electron and hole systems*, volume 41. Springer, 2003.

[66] Sergey Bravyi, David P DiVincenzo, and Daniel Loss. Schrieffer–wolff transformation for quantum many-body systems. *Annals of physics*, 326(10):2793–2826, 2011.

[67] Rukhsan Ul Haq and Keshav Singh. A systematic method for schrieffer-wolff transformation and its generalizations. *arXiv preprint arXiv:2004.06534*, 2020.

[68] Sandoko Kosen, Hang-Xi Li, Marcus Rommel, Robert Rehammar, Marco Caputo, Leif Grönberg, Jorge Fernández-Pendás, Anton Frisk Kockum, Janka Biznárová, Liangyu Chen, et al. Signal crosstalk in a flip-chip quantum processor. *PRX Quantum*, 5(3):030350, 2024.

[69] J Robert Johansson, Paul D Nation, and Franco Nori. Qutip: An open-source python framework for the dynamics of open quantum systems. *Computer physics communications*, 183(8):1760–1772, 2012.

[70] J.R. Johansson, P.D. Nation, and Franco Nori. Qutip 2: A python framework for the dynamics of open quantum systems. *Computer Physics Communications*, 184(4):1234–1240, 2013.

A

Appendix

A.1 Transmon

In reality, a typical transmon also includes a gate capacitor C_g and voltage source V_g connecting to the superconductor island, which is also connected to a reservoir supplying Cooper pairs via a Josephson junction on the other side.

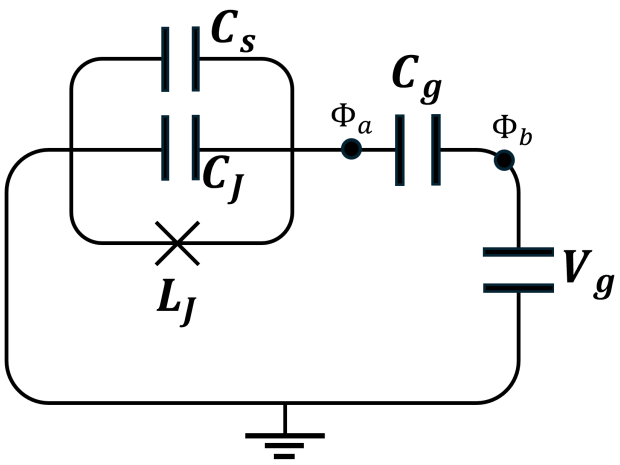

Figure A.1: The circuit diagram of a tunable transmon. C_s, C_g, and C_J are the capacitance of the shunted element, gate, and Josephson junction with inductance L_J. V_g is the voltage supplied.

We now derive the Hamiltonian for the circuit shown in Fig. A.1. For this specific spanning tree transversing the node fluxes Φ_a and Φ_b, the branch fluxes of each circuit element are:

$$\Phi_{L_J} = \Phi_a, \tag{A.1}$$
$$\Phi_{C_J} = -\Phi_a, \tag{A.2}$$
$$\Phi_g = \Phi_b - \Phi_a, \tag{A.3}$$
$$\Phi - \Phi_{C_s} = -\Phi_a, \tag{A.4}$$
$$\Phi_{V_g} = \Phi_b. \tag{A.5}$$

In this case, the capacitive energy is stored in three capacitive elements and the two

parallel capacitors form a single capacitor with $C_p = C_s + C_J$:

$$\begin{aligned} T &= \frac{1}{2}C_J\dot{\Phi}_{C_J}^2 + \frac{1}{2}C_s\dot{\Phi}_s^2 + \frac{1}{2}C_g\dot{\Phi}_g^2 \\ &= \frac{1}{2}C_p\dot{\Phi}_a^2 + \frac{1}{2}C_g(\dot{\Phi}_b - \dot{\Phi}_a)^2. \end{aligned} \tag{A.6}$$

Since the voltage supplied for a source is constant, the branch flux across it remains constant with $\dot{\Phi}_b = V_g$. Therefore, there is only one degree of freedom in T:

$$T = \frac{1}{2}C_p\dot{\Phi}_a^2 + \frac{1}{2}C_g(\dot{\Phi}_a - V_g)^2. \tag{A.7}$$

The inductive energy stored in DC-SQUID:

$$V = -E_J(\varphi_{\text{ext}})\cos(2\pi\Phi_a/\Phi_0), \tag{A.8}$$

and we have the Lagrangian expressed in $\Phi = \Phi_a$:

$$\mathcal{L} = T - V = \frac{1}{2}C_p\dot{\Phi}^2 + \frac{1}{2}C_g(\dot{\Phi} - V_g)^2 + E_J(\varphi_{\text{ext}})\cos(2\pi\Phi/\Phi_0). \tag{A.9}$$

Similarly, the variable for charge conjugated to $\dot{\Phi}$ is

$$Q = \frac{\partial\mathcal{L}}{\partial\dot{\Phi}} = C_\Sigma\dot{\Phi} - C_gV_g. \tag{A.10}$$

Scale these two conjugate coordinates with the factor $1/(2e)$ leading to new coordinates:

$$N_{\text{net}} = \frac{C_\Sigma\dot{\Phi}}{2e} - \frac{C_gV_g}{2e} = N - N_g, \tag{A.11}$$

$$\varphi = \frac{2\pi\Phi}{\Phi_0} = 2e\Phi. \tag{A.12}$$

With the new coordinates, the Lagrangian in Eq. (A.9) is rewritten as:

$$\mathcal{L} = +E_J(\varphi_{\text{ext}})\cos(\varphi). \tag{A.13}$$

We can then obtain the Hamiltonian:

$$H = N_{\text{net}}\dot{\varphi} - \mathcal{L} = 4E_C(N - N_g)^2 - E_J(\varphi_{\text{ext}})\cos(\varphi), \tag{A.14}$$

where the offset N_g is interpreted as the number of Cooper pairs taken from the island included by the gate voltage V_g. Notice that this Hamiltonian takes the same form as the Eq. (2.48), only with different E_C:

$$E_C = \frac{4e^2}{2(C_g + C_J + C_s)}. \tag{A.15}$$

It is clear that in transmon qubit, the added shunt capacitance C_s makes the ratio of E_J/E_C larger and, therefore, less sensitivity to charge noise.

A.2 2×2 Hamiltonian diagonalization

The general form of 2 by 2 Hamiltonian is:

$$H = \begin{pmatrix} h_0 + h_3 & h_1 - ih_2 \\ h_1 + ih_2 & h_0 - h_3 \end{pmatrix} \tag{A.16}$$

The Hamiltonian can be rewritten in the following form:

$$\begin{aligned} H &= h_0\sigma_0 + h_1\sigma_1 + h_2\sigma_2 + h_3\sigma_3 \\ &= h_0 I + \boldsymbol{h} \cdot \boldsymbol{\sigma}. \end{aligned} \tag{A.17}$$

The eigenvalues for H are $h_0 + h$ and $h_0 - h$:

$$H \left|h_\pm\right\rangle = (h_0 \pm h) \left|h_\pm\right\rangle, \tag{A.18}$$

where $h = \sqrt{\boldsymbol{h} \cdot \boldsymbol{h}} = \sqrt{h_1^2 + h_2^2 + h_3^2}$. Without loss of generality, one can assume $\boldsymbol{h} \cdot \boldsymbol{h} = 1$, the eigen states obtained:

$$\left|h_\pm\right\rangle = \begin{pmatrix} \sqrt{\frac{1 \pm h_3}{2}} \\ \pm\sqrt{\frac{1}{2(1 \pm h_3)}}(h_1 + ih_2) \end{pmatrix} \cdot e^{i\alpha} \tag{A.19}$$

$$= \begin{pmatrix} \sqrt{\frac{1 \pm h_3}{2}} \\ \pm\sqrt{\frac{1 \mp h_3}{2}} e^{i\phi} \end{pmatrix} \tag{A.20}$$

Given the constraint that $h_1^2 + h_2^2 = 1 - h_3^2$:

$$h_1 = \sqrt{1 - h_3^2}\cos\phi \tag{A.21}$$

$$h_2 = \sqrt{1 - h_3^2}\sin\phi \tag{A.22}$$

$$\phi = \arctan(h_2/h_1). \tag{A.23}$$

Let set $h_3 = \cos\theta$, the eigenstates are:

$$\left|h_+\right\rangle = \begin{pmatrix} \cos\frac{1}{2}\theta \\ +\sin\frac{1}{2}\theta \cdot e^{i\phi} \end{pmatrix}, \ \left|h_-\right\rangle = \begin{pmatrix} \sin\frac{1}{2}\theta \\ -\cos\frac{1}{2}\theta \cdot e^{i\phi} \end{pmatrix}. \tag{A.24}$$

A.3 Derivation of local adiabaticity condition for two-level system

We first start with the Hamiltonian for the two-level system:

$$\begin{aligned} H_{\text{tls}}(t) &= \frac{\Delta_{qc}(t)}{2}\hat{\sigma}_z + g\hat{\sigma}_x \\ &= \begin{pmatrix} \frac{\Delta_{qc}(t)}{2} & g_{qc} \\ g_{qc} & -\frac{\Delta_{qc}(t)}{2} \end{pmatrix}. \end{aligned} \tag{A.25}$$

The general form for this kind of Hamiltonian is:

$$H_{\text{tls}} = \begin{pmatrix} M_3 & M_1 \\ M_1 & -M_3 \end{pmatrix}, \tag{A.26}$$

where $M_3 = \Delta_{qc}(t)/2$ and $M_1 = g_{qc}$. The Hamiltonian can be normalized by the factor $\mathcal{N} = \sqrt{M_1^2 + M_3^2}$. The normalized Hamiltonian $\bar{H}_{qc} = H_{qc}/\mathcal{N}$ reads:

$$\bar{H}_{\text{tls}} = \begin{pmatrix} m_3 & m_1 \\ m_1 & -m_3 \end{pmatrix}. \tag{A.27}$$

The matrix elements are obtained by $m_i = M_i/\mathcal{N}$, and $m_1^2 + m_3^2 = 1$. From Appendix A.2, the eigenstates and their energies of $\bar{H}_{qc}$ are:

$$|\psi_0(t)\rangle = \begin{pmatrix} \sin(\theta/2) \\ -\cos(\theta/2) \end{pmatrix}, \tag{A.28}$$

$$|\psi_1(t)\rangle = \begin{pmatrix} \cos(\theta/2) \\ \sin(\theta/2) \end{pmatrix}, \tag{A.29}$$

$$\bar{E}_0 = -\sqrt{m_1^2 + m_3^2}, \tag{A.30}$$

$$\bar{E}_1 = +\sqrt{m_1^2 + m_3^2}, \tag{A.31}$$

where the parameter θ, m_1 and m_3 is related by $m_1 = \sin\theta$ and $m_3 = \cos\theta$. The eigen energies of H_{qc} are:

$$E_0 = \mathcal{N}\bar{E}_0 = -\sqrt{M_1^2 + M_3^2}, \tag{A.32}$$

$$E_1 = \mathcal{N}\bar{E}_1 = +\sqrt{M_1^2 + M_3^2}. \tag{A.33}$$

The square of the energy gap is:

$$|E_1 - E_0| = 2\sqrt{M_1^2 + M_3^2}. \tag{A.34}$$

Notice that the eigenstates of $\bar{H}_{\text{tls}}$ are also the eigenstates of H_{tls}, therefore we have:

$$|\langle\psi_1|\hat{\sigma}_z|\psi_0\rangle| = \sin\theta = m_1. \tag{A.35}$$

The local adiabaticity condition at any time t is:

$$\left|\frac{\partial\Delta(t)}{\partial t}\right| \ll \frac{2|E_1(t) - E_0(t)|^2}{|\langle\psi_1(t)|\hat{\sigma}_z|\psi_0(t)\rangle|} = \frac{8(M_1^2 + M_3^2)\sqrt{M_1^2 + M_3^2}}{M_1}. \tag{A.36}$$

We now arrive at the condition given qubit-coupler detuning Δ and their effective coupling rate g:

$$\left|\frac{\partial\Delta}{\partial t}\right| \ll \frac{(\Delta^2 + 4g^2)^{3/2}}{g}. \tag{A.37}$$

A.4 Derivation of local adiabaticity condition for three-level system

For a three-level system described by a Hamiltonian in the rotating frame:

$$H(t) = \begin{pmatrix} 0 & \sqrt{2}g & 0 \\ \sqrt{2}g & \Delta(t) & \sqrt{2}g \\ 0 & \sqrt{2}g & \delta(t) \end{pmatrix}, \tag{A.38}$$

where $\delta(t) = -2\Delta_{qc}(t) + \beta - \alpha$ and $\Delta(t) = -\Delta_{qc}(t) - \alpha$. The time derivative of this Hamiltonian:

$$\frac{\partial H(t)}{\partial t} = \begin{pmatrix} 0 & 0 & 0 \\ 0 & -\partial_t \Delta_{qc} & 0 \\ 0 & 0 & -2\partial_t \Delta_{qc} \end{pmatrix} = -\partial_t \Delta_{qc} \begin{pmatrix} 0 & 0 & 0 \\ 0 & 1 & 0 \\ 0 & 0 & 2 \end{pmatrix}, \tag{A.39}$$

The local adiabaticity condition for the two lowest two eigenstates is posed to the evolution:

$$\left| \langle \psi_1(t) | \frac{\partial H(t)}{\partial t} | \psi_0(t) \rangle \right| \ll |E_1(t) - E_0(t)|^2. \tag{A.40}$$

We then arrive at a differential equation for time-dependent qubit-coupler detuning $\Delta_{qc}(t)$ with an undetermined scaling prefactor γ (ranging from 0 to 1):

$$\left| \frac{\partial \Delta_{qc}}{\partial t} \right| = \gamma \frac{(E_1(t) - E_0(t))^2}{|\langle \psi_1(t) | A | \psi_0(t) \rangle|}, \tag{A.41}$$

$$A = \begin{pmatrix} 0 & 0 & 0 \\ 0 & 1 & 0 \\ 0 & 0 & 2 \end{pmatrix}. \tag{A.42}$$

A.5 Effective two-level system Hamiltonian of a three-level system using NPAD

Our goal is to derive the following effective TLS Hamiltonian:

$$H = \begin{pmatrix} \chi\Delta & \chi g_{\text{eff}} \\ \chi g_{\text{eff}} & -\chi\Delta \end{pmatrix}. \tag{A.43}$$

First, we start with the dynamics of $|f\rangle$-state reset is described by a three-by-three Hamiltonian:

$$H_0 = \begin{pmatrix} \Delta & 0 & g \\ 0 & -\Delta & g \\ g & g & \delta \end{pmatrix}, \tag{A.44}$$

where the diagonal elements Δ and δ are defined as:

$$\Delta = \omega_q - \omega_c + \alpha/2, \tag{A.45}$$

$$\delta = -\alpha/2. \tag{A.46}$$

In the first step, our goal is to eliminate the inter-coupling elements g at entries $(0,2)$ and $(2,0)$ in the Hamiltonian $H^{(0)}$:

$$H^{(0)} = H_0 - \frac{\Delta+\delta}{2} I = \begin{pmatrix} \frac{\Delta}{2} - \frac{\delta}{2} & 0 & g \\ 0 & -\frac{3\Delta}{2} - \frac{\delta}{2} & g \\ g & g & -\frac{\Delta}{2} + \frac{\delta}{2} \end{pmatrix} \tag{A.47}$$
$$= \begin{pmatrix} \Delta_1 & 0 & g \\ 0 & -\frac{3\Delta}{2} - \frac{\delta}{2} & g \\ g & g & -\Delta_1 \end{pmatrix}.$$

By applying the first Givens rotation R_1:

$$R_1 = \begin{pmatrix} \cos\left(\frac{\arctan(g/\Delta_1)}{2}\right) & 0 & \sin\left(\frac{\arctan(g/\Delta_1)}{2}\right) \\ 0 & 1 & 0 \\ -\sin\left(\frac{\arctan(g/\Delta_1)}{2}\right) & 0 & \cos\left(\frac{\arctan(g/\Delta_1)}{2}\right) \end{pmatrix}, \tag{A.48}$$

the Hamiltonian $H^{(1)}$ is obtained by transformation $H^{(1)} = R_1 H^{(0)} R_1^\dagger$:

$$H^{(1)} = \begin{pmatrix} -\sqrt{\Delta_1^2 + g^2} & g\sin\left(\frac{\arctan(g/\Delta_1)}{2}\right) & 0 \\ g\sin\left(\frac{\arctan(g/\Delta_1)}{2}\right) & -3\Delta_1 - 2\delta_1 & g\cos\frac{\arctan(g/\Delta_1)}{2}\Big) \\ 0 & g\cos\left(\frac{\arctan(g/\Delta_1)}{2}\right) & \sqrt{\Delta_1^2 + g^2} \end{pmatrix}. \tag{A.49}$$

By adding an energy offset $-\left[(H^{(1)})_{1,1} + (H^{(1)})_{2,2}\right]/2$ and define $\Delta_2 = \frac{3\Delta_1}{2} + \frac{\sqrt{\Delta_1^2+g^2}}{2} + \delta_1$, $s_1 = \sin\left(\frac{\arctan(g/\Delta_1)}{2}\right)$, $c_1 = \cos\left(\frac{\arctan(g/\Delta_1)}{2}\right)$, $H^{(1)}$ can be rewritten as

$$H^{(1)} = \begin{pmatrix} \frac{3\Delta_1}{2} + \delta_1 - \frac{3\sqrt{\Delta_1^2+g^2}}{2} & s_1 g & 0 \\ s_1 g & -\Delta_2 & c_1 g \\ 0 & c_1 g & \Delta_2 \end{pmatrix}. \tag{A.50}$$

The second Givens rotation R_2 to eliminate entries $(1,2)$ and $(2,1)$ reads:

$$R_2 = \begin{pmatrix} 1 & 0 & 0 \\ 0 & c_2 & -s_2 \\ 0 & s_2 & c_2 \end{pmatrix}, \tag{A.51}$$

$$s_2 = \sin\left(\frac{\arctan\left(c_1 g/\Delta_2\right)}{2}\right), \tag{A.52}$$

$$c_2 = \cos\left(\frac{\arctan\left(c_1 g/\Delta_2\right)}{2}\right). \tag{A.53}$$

After the second rotation, the coupling elements $c_1 g$ are eliminated, and other off-diagonal elements are modified:

$$H^{(2)} = \begin{pmatrix} \frac{3\Delta_1}{2} + \delta_1 - \frac{3\sqrt{\Delta_1^2+g^2}}{2} & s_1 c_2 g & s_1 s_2 g \\ s_1 c_2 g & -\sqrt{\Delta_2^2 + c_1^2 g^2} & 0 \\ s_1 s_2 g & 0 & \sqrt{\Delta_2^2 + c_1^2 g^2} \end{pmatrix}. \tag{A.54}$$

We can further apply more Givens rotations so that the inter-blocking coupling elements are numerically smaller than the energy difference between blocks. However, as we can see in Fig. 2.18 in the main text, two rotations are already enough to achieve a good approximation. By ignoring the elements $s_1 s_2 g$, the effective Hamiltonian from Eq. (A.54) reads ($\Delta_3 = (H^{(2)})_{0,0}/2 - (H^{(2)})_{1,1}/2$):

$$H_{\text{eff}} = \begin{pmatrix} \Delta_3 & s_1 c_2 g \\ s_1 c_2 g & -\Delta_3 \end{pmatrix} = \begin{pmatrix} \Delta_3 & g_{\text{eff}} \\ g_{\text{eff}} & -\Delta_3 \end{pmatrix}. \tag{A.55}$$

In the regime where Δ is small, we can have the following Taylor expansion of $\Delta_3 = \Delta_3(\Delta)$ and $g_{\text{eff}} = g_{\text{eff}}(\Delta)$ to the second order:

$$\Delta_3 = \left.\frac{d\Delta_3}{d\Delta}\right|_{\Delta=0} \Delta + \Delta_3(\Delta = 0) = k_1 \Delta + b_1, \tag{A.56}$$

$$g_{\text{eff}} = \left.\frac{dg_{\text{eff}}}{d\Delta}\right|_{\Delta=0} \Delta + g_{\text{eff}}(\Delta = 0) = k_2 \Delta + b_2, \tag{A.57}$$

where

$$k_1 = \left.\frac{d\Delta_3}{d\Delta}\right|_{\Delta=0}, \tag{A.58}$$

$$k_2 = \left.\frac{dg_{\text{eff}}}{d\Delta}\right|_{\Delta=0}, \tag{A.59}$$

$$b_1 = \Delta_3(\Delta = 0), \tag{A.60}$$

$$b_2 = g_{\text{eff}}(\Delta = 0). \tag{A.61}$$

Thus, We can obtain the eigenenergies given this approximation:

$$E_\pm = \pm\sqrt{(k_1^2 + k_2^2)\Delta^2 + 2(k_1 b_1 + k_2 b_2)\Delta + b_1^2 + b_2^2}. \tag{A.62}$$

By dropping the linear term in Eq. (A.62), we arrive at the expression of factor χ and effective coupling rate g_{eff} in Eq. (A.43):

$$\chi = \sqrt{k_1^2 + k_2^2}, \tag{A.63}$$

$$g_{\text{eff}} = \sqrt{\frac{b_1^2 + b_2^2}{k_1^2 + k_2^2}}. \tag{A.64}$$

DEPARTMENT OF SOME SUBJECT OR TECHNOLOGY
CHALMERS UNIVERSITY OF TECHNOLOGY
Gothenburg, Sweden
www.chalmers.se

CHALMERS
UNIVERSITY OF TECHNOLOGY